



UVCANDELS: Catalogs of Photometric Redshifts and Galaxy Physical Properties

Vihang Mehta¹ , Marc Rafelski^{2,3} , Ben Sunnquist² , Harry I. Teplitz¹ , Claudia Scarlata⁴ , Xin Wang^{5,6} ,
 Adriano Fontana⁷ , Nimish P. Hathi² , Kartheik G. Iyer⁸ , Anahita Alavi¹ , James Colbert¹ , Norman Grogin² ,
 Anton Koekemoer² , Kalina V. Nedkova^{2,3} , Matthew Hayes⁹ , Laura Prichard² , Brian Siana¹⁰ , Brent M. Smith¹¹ ,
 Rogier Windhorst¹¹ , Teresa Ashcraft¹¹ , Micaela Bagley¹² , Ivano Baronchelli¹³ , Guillermo Barro¹⁴ , Alex Blanche¹¹ ,
 Adam Broussard¹⁵ , Timothy Carleton¹¹ , Nima Chartab¹⁶ , Alex Codoreanu¹⁷ , Seth Cohen¹¹ , Christopher Conselice¹⁸ ,
 Y. Sophia Dai⁶ , Behnam Darvish¹⁰ , Romeel Davé¹⁹ , Laura DeGroot²⁰ , Duilia De Mello²¹ , Mark Dickinson²² ,
 Najmeh Emami¹⁰ , Henry Ferguson² , Leonardo Ferreira²³ , Keely Finkelstein¹² , Steven Finkelstein¹² ,
 Jonathan P. Gardner²⁴ , Eric Gawiser¹⁵ , Timothy Gburek¹⁰ , Mauro Giavalisco²⁵ , Andrea Grazian¹³ , Caryl Gronwall²⁶ ,
 Yicheng Guo²⁷ , Pablo Arrabal Haro²² , Shoubaneh Hemmati¹ , Justin Howell¹ , Rolf A. Jansen¹¹ , Zhiyuan Ji²⁵ ,
 Sugata Kaviraj²⁸ , Keunho J. Kim¹ , Peter Kurczynski²⁴ , Ilin Lazar²⁹ , Ray A. Lucas² , John MacKenty² ,
 Kameswara Bharadwaj Mantha⁴ , Alec Martin²⁷ , Garreth Martin^{30,31} , Tyler McCabe¹¹ , Bahram Mobasher¹⁰ ,
 Alexa M. Morales¹² , Robert O'Connell³² , Charlotte Olsen¹⁵ , Lillian Otteson¹¹ , Swara Ravindranath² ,
 Caleb Redshaw¹¹ , Michael Rutkowski³³ , Brant Robertson³⁴ , Zahra Sattari¹⁰ , Emmaris Soto³⁵ , Lei Sun⁵ ,
 Sina Taamoli¹⁰ , Eros Vanzella³⁶ , L. Y. Aaron Yung² , and Bonnabelle Zabelle⁴

(The UVCANDELS Team)

¹ IPAC, Mail Code 314-6, California Institute of Technology, 1200 E. California Blvd., Pasadena, CA 91125, USA; vmehta@ipac.caltech.edu² Space Telescope Science Institute, 3700 San Martin Dr., Baltimore, MD 21218, USA³ Department of Physics and Astronomy, Johns Hopkins University, Baltimore, MD 21218, USA⁴ Minnesota Institute for Astrophysics, University of Minnesota, 116 Church St. SE, Minneapolis, MN 55455, USA⁵ School of Astronomy and Space Science, University of Chinese Academy of Sciences (UCAS), Beijing 100049, People's Republic of China⁶ National Astronomical Observatories, Chinese Academy of Sciences, Beijing 100101, People's Republic of China⁷ INAF—Osservatorio Astronomico di Roma—via Frascati 33, Monte Porzio Catone, 00078 Rome, Italy⁸ Columbia Astrophysics Laboratory, Columbia University, 550 West 120th St., New York, NY 10027, USA⁹ Stockholm University, Department of Astronomy and Oskar Klein Centre for Cosmoparticle Physics, SE-10691, Stockholm, Sweden¹⁰ Department of Physics and Astronomy, University of California, Riverside, Riverside, CA 92521, USA¹¹ School of Earth and Space Exploration, Arizona State University, Tempe, AZ 85287, USA¹² Department of Astronomy, The University of Texas at Austin, Austin, TX 78712, USA¹³ INAF—Osservatorio Astronomico di Padova, Vicolo dell'Osservatorio 5, I-35122, Padova, Italy¹⁴ Department of Physics, University of the Pacific, Stockton, CA 95211, USA¹⁵ Department of Physics and Astronomy, Rutgers, The State University of New Jersey, Piscataway, NJ 08854, USA¹⁶ Observatories of the Carnegie Institution of Washington, Pasadena, CA 91101, USA¹⁷ Centre for Astrophysics and Supercomputing, Swinburne University of Technology, Hawthorn, VIC 3122, Australia¹⁸ School of Physics and Astronomy, The University of Nottingham, University Park, Nottingham, NG7 2RD, UK¹⁹ Institute for Astronomy, University of Edinburgh, Edinburgh, EH9 3HJ, UK²⁰ College of Wooster, Wooster, OH 44691, USA²¹ Department of Physics, The Catholic University of America, Washington, DC 20064, USA²² NSF's NOIRLab, Tucson, AZ 85719, USA²³ Centre for Astronomy and Particle Physics, School of Physics and Astronomy, University of Nottingham, NG7 2RD, UK²⁴ Astrophysics Science Division, NASA Goddard Space Flight Center, Greenbelt, MD 20771, USA²⁵ Department of Astronomy, University of Massachusetts, Amherst, MA 01003, USA²⁶ Department of Astronomy & Astrophysics, The Pennsylvania State University, University Park, PA 16802, USA²⁷ Department of Physics and Astronomy, University of Missouri, Columbia, MO 65211, USA²⁸ Centre for Astrophysics Research, University of Hertfordshire, Hatfield, AL10 9AB, UK²⁹ Department of Galaxies and Cosmology, Max Planck Institute for Astronomy, Königstuhl 17, 69117 Heidelberg, Germany³⁰ Korea Astronomy and Space Science Institute, Yuseong-gu, Daejeon 34055, Republic of Korea³¹ Steward Observatory, University of Arizona, Tucson, AZ 85719, USA³² Department of Astronomy, University of Virginia, Charlottesville, VA 22904, USA³³ Department of Physics and Astronomy, Minnesota State University Mankato, Mankato, MN 56001, USA³⁴ Department of Astronomy and Astrophysics, University of California, Santa Cruz, CA 95064, USA³⁵ Computational Physics, Inc., Springfield, VA 22151, USA³⁶ INAF—Osservatorio di Astrofisica e Scienza dello Spazio di Bologna, via Gobetti 93/3, I-40129 Bologna, Italy

Received 2024 July 4; revised 2024 August 30; accepted 2024 September 4; published 2024 November 8

Abstract

The UltraViolet imaging of the Cosmic Assembly Near-infrared Deep Extragalactic Legacy Survey Fields (UVCANDELS) program provides deep Hubble Space Telescope (HST) F275W and F435W imaging over four CANDELS fields (GOODS-N, GOODS-S, COSMOS, and Extended Groth Strip). We combine this newly acquired UV imaging with existing HST imaging from CANDELS as well as existing ancillary data to obtain



Original content from this work may be used under the terms of the [Creative Commons Attribution 4.0 licence](https://creativecommons.org/licenses/by/4.0/). Any further distribution of this work must maintain attribution to the author(s) and the title of the work, journal citation and DOI.

robust photometric redshifts and reliable estimates for galaxy physical properties for over 150,000 galaxies in the $\sim 430 \text{ arcmin}^2$ UVCANDELS area. Here, we leverage the power of the new UV photometry to not only improve the photometric redshift measurements in these fields, but also constrain the full redshift probability distribution combining multiple redshift-fitting tools. Furthermore, using the full UV-to-IR photometric data set, we measure the galaxy physical properties by fitting templates from population synthesis models with two different parameterizations (flexible and fixed form) of the star formation histories (SFHs). Compared to the flexible SFH parameterization, we find that the fixed-form SFHs systematically underestimate the galaxy stellar masses, both at the low-mass ($\lesssim 10^9 M_\odot$) and high-mass ($\gtrsim 10^{10} M_\odot$) end, by as much as ~ 0.5 dex. This underestimation is primarily due the limited ability of fixed-form SFH parameterization to simultaneously capture the chaotic nature of star formation in these galaxies.

Unified Astronomy Thesaurus concepts: [Catalogs \(205\)](#); [Galaxies \(573\)](#); [Astronomical methods \(1043\)](#)

1. Introduction

Over the past few decades, our knowledge of galaxy formation and evolution has seen significant advancement and large multiwavelength photometric surveys have been one of the cornerstones enabling this progress. Space-based facilities such as Hubble Space Telescope (HST), Spitzer, and now JWST have granted access not only to high-resolution and extremely sensitive imaging, but also to wavelengths that are otherwise inaccessible from the ground. The combination of space- and ground-based observations covering wavelengths from the far-ultraviolet (UV) out to mid-infrared (IR) have facilitated detailed studies of galaxies and the physical processes that govern how they grow and evolve over time—namely, tracing the evolution of the stellar mass function over time (e.g., D. Marchesini et al. 2009; A. Muzzin et al. 2013; I. Davidzon et al. 2017; J. R. Weaver et al. 2023; A. Weibel et al. 2024), the cosmic star formation rate and its evolution (e.g., A. Alavi et al. 2014, 2016; P. Madau & M. Dickinson 2014; V. Mehta et al. 2017; T. Moutard et al. 2020; V. Picouet et al. 2023), the star-forming main sequence (e.g., J. S. Speagle et al. 2014; K. E. Whitaker et al. 2014; P. Kurczynski et al. 2016; L. A. Boogaard et al. 2018; R. M. Mérida et al. 2023), and the mass–size relation (e.g., S. Shen et al. 2003; I. K. Baldry et al. 2012; T. Morishita et al. 2017; K. V. Nedkova et al. 2021, 2024), among others. In particular, the WFC3/UVIS instrument on board HST has been monumental by providing access to the rest-frame UV light from galaxies, which is key for studying their star formation properties and hence tracking their growth as well as for constraining the amount of dust in them.

One such pivotal photometric survey has been the Cosmic Assembly Near-infrared Deep Extragalactic Legacy Survey (CANDELS; N. A. Grogin et al. 2011; A. M. Koekemoer et al. 2011), which is a legacy HST program that obtained WFC3/IR and Advanced Camera for Surveys Wide Field Channel (ACS/WFC) optical imaging in up to 10 broadband filters for five extragalactic fields (GOODS-N, GOODS-S, COSMOS, Extended Groth Strip (EGS), and Ultra Deep Survey) over a combined area of $\sim 0.2 \text{ deg}^2$. Complemented with additional observations with Spitzer and various other ground-based instruments, the CANDELS fields serve as one of the premier observational data sets for studying galaxy evolution and have already enabled a wide range of science. The CANDELS team has previously assembled catalogs that include multiwavelength photometric coverage for the HST as well as all ancillary data available on these fields (Y. Guo et al. 2013; H. Nayyeri et al. 2017; M. Stefanon et al. 2017; G. Barro et al. 2019).

Recently, another HST Treasury campaign, UltraViolet imaging of the Cosmic Assembly Near-infrared Deep Extragalactic Legacy Survey Fields (UVCANDELS; PI: H. Teplitz; PID: 15647; X. Wang et al. 2024), accomplished the task of obtaining UV imaging with F275W and F435W (in parallel) over four of the five CANDELS fields (GOODS-N, GOODS-S, COSMOS, EGS). The new F435W coverage in COSMOS and EGS fields overlaps with that of F275W which previously did not have F435W; while in GOODS-N and GOODS-S, the parallel F435W coverage is limited to the deeper regions (not overlapping with F275W) given the existing F435W data already available for the UVCANDELS regions. The additional UV coverage improves the photometric-redshift estimates, particularly for objects that have degenerate solutions, typically characterized as multiple peaks in their photometric-redshift probability distributions that are significant (e.g., $\gtrsim 10\%$ of the primary peak) and sufficiently separated in redshift (e.g., $\Delta z/(1+z) \gtrsim 0.06$), which when not appropriately accounted for can lead to catastrophic errors in the measured redshifts and associated uncertainties (e.g., M. Rafelski et al. 2009, 2015). The UV imaging helps prevent this for example by sampling the Lyman break of $z \sim 2$ galaxies removing the degeneracy with the Balmer break of $z \sim 0.3$ galaxies. Similarly, the UV photometry is critical to accurately constrain the recent star formation activity and dust content of galaxies (e.g., V. Mehta et al. 2017, 2023). In this work, we leverage the existing multiwavelength CANDELS photometry with the addition of the new F275W and F435W photometry from UVCANDELS to provide improved photometric redshifts as well as galaxy physical properties for over 150,000 galaxies in these four CANDELS fields.

Estimating both photometric redshifts and physical parameters via modeling the galaxy spectral energy distribution (SED) has been well established with a vast library of tools with varying levels of sophistication now available for both (e.g., M. Rafelski et al. 2015; V. Mehta et al. 2018; D. Kodra et al. 2023; C. Pacifici et al. 2023). However, variations in template choices and codes result in slightly different results (e.g., T. Dahlen et al. 2013). In this work, we leverage the power of multiple photometric-redshift-fitting tools and template sets and combine their results to yield robust redshift estimates as well as to accurately quantify the redshift probability distributions. When estimating the galaxy physical properties, the star formation history (SFH) plays an essential role in determining the galaxy SED (e.g., K. G. Iyer et al. 2019; J. Leja et al. 2019) and traditionally SFHs in typical SED-fitting tools have been assumed to have fixed, functional forms. However, there is increasing evidence suggesting that galaxy

SFHs, particularly in the early Universe as well as toward the low-mass end, are not smoothly evolving; rather they are chaotic and often bursty in nature, both from theoretical (see, e.g., P. F. Hopkins et al. 2014; A. Domínguez et al. 2015; G. Sun et al. 2023) as well as observational perspectives (see, e.g., D. R. Weisz et al. 2012; V. Mehta et al. 2017, 2023; N. Emami et al. 2019). In this work, we explore the impact of the traditional fixed-form SFH assumption for even the most basic physical parameter—i.e., galaxy stellar mass—by comparing to results from fitting tools that accommodate more flexible forms for the galaxy SFH.

This article is organized as follows: Section 2 describes the UVCANDELS data set as well as the ancillary photometric data sets used for this analysis, Section 3 describes the techniques used for estimating photometric redshifts and discusses the improvement in the redshift estimates by the inclusion of the UV photometry, Section 4 describes the methodologies used for the measurements of galaxy physical parameters and discusses the impact of the fixed versus flexible-form for the galaxy SFHs on the estimated physical parameters, Section 5 describes the final output catalogs that present the various measurements from this work and presents the publicly released catalogs, and Section 6 summarizes our findings.

Throughout this paper, we adopt cosmological parameters from Table 3 of Planck Collaboration et al. (2016): $\Omega_m = 0.315$, $\Omega_\lambda = 0.685$, and $H_0 = 67.31 \text{ km s}^{-1} \text{ Mpc}^{-1}$. All magnitudes used are AB magnitudes (J. B. Oke & J. E. Gunn 1983).

2. Data

2.1. UVCANDELS Imaging

The UVCANDELS (PI: H. Teplitz; PID: 15647; X. Wang et al. 2024) is a Cycle 26 Hubble Treasury program that obtained WFC3/UVIS F275W and ACS/WFC F435W (in parallel) for four of the deep-wide survey fields defined by CANDELS (N. A. Grogin et al. 2011; A. M. Koekemoer et al. 2011), namely GOODS-N, GOODS-S, COSMOS, and EGS, covering a combined area of $\sim 430 \text{ arcmin}^2$. The UVCANDELS imaging reaches a depth of $AB = 27$ for compact galaxies in the WFC3/UVIS F275W filter, and $AB \leq 28$ in ACS/F435W. The UVCANDELS F275W mosaics are available at the Mikulski Archive for Space Telescopes (MAST; doi:10.17909/8s31-f778) for all four fields along with EGS.³⁷ These UVCANDELS image mosaics are aligned and registered to the CANDELS astrometry. With the newly acquired UVCANDELS imaging, we have measured the fluxes in the F275W filter for the four fields and F435W for COSMOS and EGS. See X. Wang et al. (2024) and L. Sun et al. (2024) for full details on the methodology to generate the mosaics and photometric catalogs, respectively.

2.2. Photometric Data Sets

The photometric data set used for modeling the galaxy SEDs in this work are primarily based on the publicly available CANDELS catalogs (S. Faber 2011), with the addition of the new F275W and F435W UVCANDELS photometry. Specifically, the CANDELS multiwavelength photometric catalogs

that we use for GOODS-N, GOODS-S, COSMOS, and EGS fields are described and presented in Y. Guo et al. (2013), H. Nayyeri et al. (2017), G. Barro et al. (2019), and M. Stefanon et al. (2017), respectively. Similarly, the photometric techniques used for measuring the F275W and F435W fluxes as well as the catalogs from UVCANDELS are fully described in detail in L. Sun et al. (2024). These F275W and F435W fluxes from UVCANDELS are measured in a consistent fashion like the rest of the CANDELS photometry (see Section 2.3 for more details). For completeness, we briefly summarize the various surveys that make up the full photometric data set for each field in the subsections below as well as in Table 1.

2.2.1. GOODS-N

We use the photometric catalog from G. Barro et al. (2019) for the GOODS-N field (M. Giavalisco et al. 2004). For the SED modeling, we consider the photometry for HST/ACS optical imaging in F435W, F606W, F775W, F814W, and F850LP from the GOODS HST/ACS Treasury Program (M. Giavalisco et al. 2004), the CANDELS survey (N. A. Grogin et al. 2011; A. M. Koekemoer et al. 2011), as well as the search for high-redshift Type Ia supernovae (e.g., A. G. Riess et al. 2007). We include photometry for HST/WFC3 imaging in the near-IR (NIR) filters F105W, F125W, and F160W from the CANDELS survey as well as additional F140W coverage from the G141 AGHAST survey (B. Weiner et al. 2009). We further include the new HST/WFC3 F275W photometry available from the UVCANDELS imaging (L. Sun et al. 2024; X. Wang et al. 2024).

In addition to the HST imaging, we also use the ground-based LBT/LBC U' -band photometry from A. Grazian et al. (2017) as well as the K_s -band photometry from Subaru/MOIRCS (M. Kajisawa et al. 2011) and CFHT/WIRCam (L.-T. Hsu et al. 2019). Lastly, we include Spitzer/IRAC ch. 1 ($3.6 \mu\text{m}$), 2 ($4.5 \mu\text{m}$), 3 ($5.8 \mu\text{m}$), and 4 ($8.0 \mu\text{m}$) photometry available from a combination of the Spitzer Extended Deep Survey (SEDS; M. L. N. Ashby et al. 2013), the Spitzer-CANDELS (S-CANDELS; M. L. N. Ashby et al. 2015), and Spitzer-GOODS (M. Dickinson et al. 2003) surveys.

2.2.2. GOODS-S

Y. Guo et al. (2013) present in full detail the photometric catalog that we use for the GOODS-S field. Similar to GOODS-N, the photometry for HST/ACS F435W, F606W, F775W, F814W, and F850LP is provided from the GOODS HST/ACS Treasury Program, the CANDELS survey, as well as the search for high-redshift Type Ia supernovae. The HST/WFC3 photometry for F098M, F105W, F125W, and F160W is provided from the CANDELS, Hubble Ultra-Deep Field (HUDF; R. J. Bouwens et al. 2010), and Early Release Science (R. A. Windhorst et al. 2011) programs. Critically, we add the new HST/WFC3 F275W photometry from UVCANDELS (L. Sun et al. 2024; X. Wang et al. 2024).

Furthermore, photometry from ground-based imaging in the U band from Blanco/MOSAIC II and Very Large Telescope (VLT)/VIMOS (M. Nonino et al. 2009) is included as well as the K_s band from VLT/ISAAC (J. Retzlaff et al. 2010) and VLT/HAWK I (A. Fontana et al. 2014). Lastly, Spitzer/IRAC ch. 1, 2, 3, and 4 photometry available from a combination of

³⁷ The F435W mosaics for GOODS-N and GOODS-S covered by UVCANDELS are already available from CANDELS.

Table 1

The Set of Photometric Filters Included for SED Modeling, Both when Measuring the Photometric Redshifts as well as the Galaxy Physical Parameters

Field	Instrument	Filter	Survey/Reference
GOODS-N ^a	HST/UVIS	F275W ^b	UVCANDELS (L. Sun et al. 2024; X. Wang et al. 2024)
	HST/ACS	F435W, F606W, F775W, F814W, F850LP	GOODS (M. Giavalisco et al. 2004), CANDELS (N. A. Grogin et al. 2011; A. M. Koekemoer et al. 2011), A. G. Riess et al. (2007)
	HST/WFC3	F105W, F125W, F140W, F160W	CANDELS (N. A. Grogin et al. 2011; A. M. Koekemoer et al. 2011), AGHAST (B. Weiner et al. 2009)
	LBT/LBC	U'	A. Grazian et al. (2017)
	Subaru/MOIRCS	K_s	M. Kajisawa et al. (2011)
	CFHT/WIRCam	K_s	L.-T. Hsu et al. (2019)
	Spitzer/IRAC	ch. 1, 2, 3, 4	SEDS (M. L. N. Ashby et al. 2013), S-CANDELS (M. L. N. Ashby et al. 2015), Spitzer-GOODS (M. Dickinson et al. 2003)
GOODS-S ^a	HST/UVIS	F275W ^b	UVCANDELS (L. Sun et al. 2024; X. Wang et al. 2024)
	HST/ACS	F435W, F606W, F775W, F814W, F850LP	GOODS (M. Giavalisco et al. 2004), CANDELS (N. A. Grogin et al. 2011; A. M. Koekemoer et al. 2011), A. G. Riess et al. (2007)
	HST/WFC3	F098M, F105W, F125W, F160W	CANDELS (N. A. Grogin et al. 2011; A. M. Koekemoer et al. 2011), HUDF (R. J. Bouwens et al. 2010), ERS (R. A. Windhorst et al. 2011)
	Blanco/MOSAIC II	U	Y. Guo et al. (2013)
	VLT/VIMOS	U	M. Nonino et al. (2009)
	VLT/ISAAC	K_s	J. Retzlaff et al. (2010)
	VLT/HAWK-I	K_s	A. Fontana et al. (2014)
	Spitzer/IRAC	ch. 1, 2, 3, 4	SEDS (M. L. N. Ashby et al. 2013), Spitzer-GOODS (M. Dickinson et al. 2003)
	COSMOS ^a	HST/UVIS	F275W ^b
HST/ACS		F435W ^b , F606W, F814W	UVCANDELS (L. Sun et al. 2024; X. Wang et al. 2024), CANDELS (N. A. Grogin et al. 2011; A. M. Koekemoer et al. 2011)
HST/WFC3		F125W, F160W	CANDELS (N. A. Grogin et al. 2011; A. M. Koekemoer et al. 2011)
CFHT/MegaPrime		$ugriz$	CHFT-LS (S. D. J. Gwyn 2012)
Subaru/Suprime-Cam		$Bg^+Vr^+i^+z^+$	Y. Taniguchi et al. (2007, 2015)
VISTA/VIRCAM		$YJHK_s$	UltraVISTA (H. J. McCracken et al. 2012)
Mayall/NEWFIRM		$J1, J2, J3, H1, H2, K$	NMBS (K. E. Whitaker et al. 2011)
Spitzer/IRAC		ch. 1, 2, 3, 4	SEDS (M. L. N. Ashby et al. 2013), S-COSMOS (D. B. Sanders et al. 2007)
EGS ^a	HST/UVIS	F275W ^b	UVCANDELS (L. Sun et al. 2024; X. Wang et al. 2024)
	HST/ACS	F435W ^b , F606W, F814W	UVCANDELS (L. Sun et al. 2024; X. Wang et al. 2024), CANDELS (N. A. Grogin et al. 2011; A. M. Koekemoer et al. 2011)
	HST/WFC3	F125W, F140W, F160W	CANDELS (N. A. Grogin et al. 2011; A. M. Koekemoer et al. 2011), 3D-HST (G. B. Brammer et al. 2012; R. E. Skelton et al. 2014)
	CFHT/MegaCam	$ugriz$	CFHT-LS (S. D. J. Gwyn 2012)
	CFHT/WIRCam	JHK_s	WIRDS (R. Bielby et al. 2012)
	Mayall/NEWFIRM	$J1 J2 J3 H1 H2 K$	NMBS (K. E. Whitaker et al. 2011)
	Spitzer/IRAC	ch. 1, 2, 3, 4	SEDS (M. L. N. Ashby et al. 2013), S-CANDELS (M. L. N. Ashby et al. 2015), AEGIS (P. Barnby et al. 2008)

Notes.

^a All photometry except for that provided by UVCANDELS is from the publicly available CANDELS multiwavelength photometric catalogs—i.e., G. Barro et al. (2019) for GOODS-N, Y. Guo et al. (2013) for GOODS-S, H. Nayyeri et al. (2017) for COSMOS, and M. Stefanon et al. (2017) for EGS.

^b Photometry for the F275W (all four fields) and F435W (COSMOS and EGS) bands is the new addition from UVCANDELS (L. Sun et al. 2024; X. Wang et al. 2024).

SEDS (M. L. N. Ashby et al. 2013), and the Spitzer-GOODS (M. Dickinson et al. 2003) survey is also included.

2.2.3. COSMOS

For the COSMOS field (N. Scoville et al. 2007), we utilize the catalog from H. Nayyeri et al. (2017) for all photometry except for HST/WFC3 F275W and HST/ACS F435W which are provided from UVCANDELS (L. Sun et al. 2024; X. Wang et al. 2024). We include the photometry in HST/ACS imaging filters F606W, F814W as well as in HST/WFC3 NIR filters F125W, F140W from the CANDELS survey.

There exists a wealth of ancillary ground-based data for the COSMOS field. Here, we include the photometry from CFHT-

LS $ugriz$ bands (S. D. J. Gwyn 2012), Subaru/Suprime-Cam $Bg^+Vr^+i^+z^+$ from Y. Taniguchi et al. (2015), and VISTA/VIRCAM $YJHK_s$ from the UltraVISTA survey (H. J. McCracken et al. 2012). We also include the medium-band photometry from the NEWFIRM Medium Band Survey (NMBS; K. E. Whitaker et al. 2011) for Mayall/NEWFIRM $J1, J2, J3, H1, H2,$ and K bands. Lastly, the Spitzer/IRAC ch. 1, 2, 3, and 4 photometry from the S-COSMOS survey (D. B. Sanders et al. 2007) is also used.

2.2.4. EGS

The catalog from M. Stefanon et al. (2017) is used for all photometry in the EGS field except for HST/WFC3 F275W

and HST/ACS F435W filters which are provided from the UVCANDELS imaging (L. Sun et al. 2024; X. Wang et al. 2024). We include the photometry for HST/ACS F606W and F814W imaging taken as part of the AEGIS project and the CANDELS survey. The HST/WFC3 photometry available in the NIR filters F125W, F140W, and F160W is contributed from a combination of the CANDELS and the 3D-HST (G. B. Brammer et al. 2012) surveys.

Additionally, photometry from ground-based imaging in *ugriz* using CFHT-LS (S. D. J. Gwyn 2012) is also included alongside CFHT/WIRCam *JHK_s* imaging from the WIRCam Deep Survey (R. Bielby et al. 2012). Similar to COSMOS, we include the medium-band imaging in the Mayall/NEWMIR *J1, J2, J3, H1, H2,* and *K* bands from NMBS (K. E. Whitaker et al. 2011). Lastly, we include the Spitzer/IRAC ch. 1, 2, 3, and 4 photometry from the SEDS (M. L. N. Ashby et al. 2013), S-CANDELS (M. L. N. Ashby et al. 2015), and AEGIS (P. Barmby et al. 2008).

2.3. Photometric Measurements

While we refer the reader to the respective publications for the exact details of the photometric techniques used to assemble the multiwavelength catalogs, we briefly summarize the pertinent details here. For all the CANDELS catalogs considered here, the object detection is performed on the F160W-band image. The isophotes defined on the F160W image are then used to measure the photometry in the remaining bands. For the high-resolution data (i.e., all HST bands), the point-spread function (PSF) for each image is convolved to match the F160W resolution, which has the broadest PSF among the HST filters. For the low-resolution images (i.e., ground based and Spitzer/IRAC), the photometry was performed using the TFIT software (V. G. Laidler et al. 2007), which uses a morphological template-fitting technique.

For the F275W/F435W photometry added from the UVCANDELS imaging (L. Sun et al. 2024; X. Wang et al. 2024), the F275W and F435W magnitudes are computed using UV-optimized isophotes following the methodology from the HUDF UV (UVUDF; H. I. Teplitz et al. 2013) analysis from M. Rafelski et al. (2015). Specifically, instead of following the typical approach of performing PSF-matched photometry using the isophotes defined on images with the broadest PSF (typically F160W for HST imaging data), we use isophotes defined on the F606W image instead to measure the fluxes from the unconvolved F275W/F435W images (without matching PSF), followed by applying an adjustment factor to correct for the aperture and PSF differences to match back to the F160W isophote-based photometry. This has the advantage of having isophotes/apertures that are more appropriately matched to the detected UV sizes, and thus return significantly better signal-to-noise ratio (SNR) for the measured fluxes. In order to keep the photometry consistent with the rest from CANDELS, these F606W-defined isophotes are matched and reconciled back to the F160W isophotes used by the CANDELS photometric catalogs. This is described as the photometry from the “VtoH” segmentation maps in L. Sun et al. (2024), which also provides the full detailed description of this photometric technique and methodology.

For the SED modeling presented in this work, we use the photometry from a combination of the CANDELS and UVCANDELS catalogs described above. Before proceeding with the fitting, we correct the photometry for galactic

extinction using the D. J. Schlegel et al. (1998) dust maps.³⁸ The reddening $E(B - V)$ is queried at the position of each galaxy and converted to an extinction assuming a J. A. Cardelli et al. (1989) extinction law, for the respective filters.

3. Photometric Redshifts

There are many different photometric-redshift codes available, and they all yield slightly different results when run on the same data (e.g., T. Dahlen et al. 2013; D. Kodra et al. 2023). In this work, we opt to utilize multiple codes and combine the results, which yields more robust redshifts than any individual code due to different systematic uncertainties in the codes and choice of template spectra. Specifically, we calculate photometric redshifts by combining the results from four different codes: EAZY (G. B. Brammer et al. 2008), BPZ (D. Coe et al. 2006), LEPHARE (S. Arnouts et al. 1999; O. Ilbert et al. 2006), and ZPHOT (E. Giallongo et al. 1998; A. Fontana et al. 2000). These codes were chosen as they were consistently among the top performers in photometric-redshift review papers of CANDELS fields (H. Hildebrandt et al. 2010; T. Dahlen et al. 2013).

We run two separate iterations of EAZY (G. B. Brammer et al. 2008) to give us a total of five independent code-run results. The first EAZY iteration uses the default template spectra (`easy_v1.2_dusty`) which includes the six original templates from G. B. Brammer et al. (2008), emission lines from O. Ilbert et al. (2009), an old and red SED from C. Maraston (2005), and a dusty SED from G. Bruzual & S. Charlot (2003). The second EAZY iteration uses the five templates from M. R. Blanton & S. Roweis (2007) (`br07_default`). Both template sets use a nonnegative matrix factorization to optimally select a reduced set of spectral templates that reproduce observed data (M. R. Blanton & S. Roweis 2007). The first template set is optimized for high-redshift galaxies from theoretical models, while the second is optimized for lower redshifts based on empirical Sloan Digital Sky Survey data. For both iterations, EAZY is restricted to a redshift range 0–12.

For BPZ (N. Benítez 2000; N. Benítez et al. 2004; D. Coe et al. 2006), we use the improved software and procedure described in M. Rafelski et al. (2015), which includes 11 template SEDs based on those from PEGASE (M. Fioc & B. Rocca-Volmerange 1997) but recalibrated based on photometric and spectroscopic redshifts from FIREWORKS (S. Wuyts et al. 2008), and a prior based on luminosity functions observed in COSMOS (O. Ilbert et al. 2009), GOODS-MUSIC (A. Grazian et al. 2006; P. Santini et al. 2009), and the HUDF (D. Coe et al. 2006).

The other two codes were used with their default template sets. For LEPHARE (S. Arnouts et al. 1999; O. Ilbert et al. 2006), we use the 32 COSMOS SEDs described in O. Ilbert et al. (2009), and corrected for emission lines and extinction using the reddening laws from D. Calzetti et al. (2000) and M. L. Prevot et al. (1984). For ZPHOT (E. Giallongo et al. 1998; A. Fontana et al. 2000), we use SED templates from G. Bruzual & S. Charlot (2003) with the addition of D. Calzetti et al. (2000) extinction and X. Fan et al. (2006) absorption due to the intergalactic medium (IGM).

³⁸ Specifically, we use the Python implementation from <https://github.com/adm/SFD> to query the D. J. Schlegel et al. (1998) maps.

We note that sometimes photometric redshifts are calculated iteratively, implementing zero-point offsets to the photometry or modifying the templates based on the spectroscopic redshifts (e.g., G. Barro et al. 2019). This can often improve the photometric-redshift accuracy, although a number of the templates used in this study are already optimized based on empirical data. We found that, on average, the dispersion of the redshifts were improved by modifying the zero-points, but that it worsened the results at $z \gtrsim 3$. Also, each code would need a different set of zero-point offsets, which would add a level of inconsistency in the input photometry. We therefore opted not to modify the zero-points or modify the templates based on the spectroscopic redshifts.

3.1. Spectroscopic Redshifts

In order to test the accuracy of our photometric redshifts as well as to combine the results from the individual codes together, we require a highly vetted spectroscopic-redshift catalog. We use a compilation of publicly available spectroscopic redshifts obtained from various facilities/sources in the UVCANDELS fields. The final spectroscopic reference sample used in this analysis is assembled from a combination of the 3D-HST (G. B. Brammer et al. 2012; I. G. Momcheva et al. 2016), zCOSMOS (S. J. Lilly et al. 2007, 2009), hCOSMOS (I. Damjanov et al. 2018), PRIMUS (A. L. Coil et al. 2011), MOSDEF (M. Kriek et al. 2015), DEIMOS 10K (G. Hasinger et al. 2018), DEEP2 (J. A. Newman et al. 2013), DEEP3 (M. C. Cooper et al. 2011, 2012), MUSE-Wide (E. C. Herenz et al. 2017), MUSE-HUDF (H. Inami et al. 2017), K20 (M. Mignoli et al. 2005), C3R2 (D. C. Masters et al. 2019; S. A. Stanford et al. 2021), LEGA-C (A. van der Wel et al. 2016), VVDS (O. Le Fèvre et al. 2013), VUDS (O. Le Fèvre et al. 2015), VANDELS (R. J. McLure et al. 2018; L. Pentericci et al. 2018), GMASS (J. Kurk et al. 2013), FMOS-COSMOS (J. D. Silverman et al. 2015), FIREWORKS (S. Wuyts et al. 2008), GOODS-MUSIC (A. Grazian et al. 2006), PEARS (I. Ferreras et al. 2009; A. N. Straughn et al. 2009), GRAPES-HUDF (A. Pasquali et al. 2006; N. P. Hathi et al. 2009), and LCIRS (M. Doherty et al. 2005) spectroscopic surveys as well as compilations from the following publications: S. Cristiani et al. (2000), S. M. Croom et al. (2001), C. Wolf et al. (2004), E. Daddi et al. (2004), L.-G. Strolger et al. (2004), A. van der Wel et al. (2005), N. D. Roche et al. (2006), C. D. Ravikumar et al. (2007), A. J. Barger et al. (2008), E. Vanzella et al. (2008, 2009), E. Treister et al. (2009), J. R. Trump et al. (2009, 2011, 2013), J. S. Huang et al. (2009); S. Wuyts et al. (2009), I. Balestra et al. (2010), T. Yoshikawa et al. (2010), J. K. Krogager et al. (2014), G. D. Wirth et al. (2015), and J. R. Trump et al. (2015), including some spectroscopic redshifts provided to our team via private communications.

For our spectroscopic reference sample, we only include those redshifts with the highest data quality flags from the individual papers, and those 3D-HST grism redshifts with good grism data quality flags (`use_zgrism=1`). We omit sources with X-ray detections to avoid active galactic nucleus contaminants, (Y. Q. Xue et al. 2016; D. Kocevski 2023, private communication), which amounts to a total of 858 objects excluded. To avoid potential confusion from neighbors in ground-based spectroscopy, we also exclude any sources that have a relatively bright neighbor, defined as a source within $3''$ and within 2 mag or brighter in F160W. As a final measure to ensure only the highest quality redshifts remain, we visually

Table 2
Column Descriptions for the Photometric-redshift Catalog

No.	Parameter	Description
1	field	The CANDELS field
2	id	The CANDELS ID
3	RA	R.A.
4	DEC	Decl.
5	photz	Best photometric redshift
6	l68	Lower 68.3% confidence interval of photz
7	u68	Upper 68.3% confidence interval of photz
8	zpeak	Highest $P(z)$ peak
9	zpeak_l68	Lower 68.3% confidence interval of zpeak
10	zpeak_u68	Upper 68.3% confidence interval of zpeak
11	zpeak2	Second highest $P(z)$ peak
12	zpeak2_l68	Lower 68.3% confidence interval of zpeak2
13	zpeak2_u68	Upper 68.3% confidence interval of zpeak2
14	zpeak3	Third highest $P(z)$ peak
15	zpeak3_l68	Lower 68.3% confidence interval of zpeak3
16	zpeak3_u68	Upper 68.3% confidence interval of zpeak3
17	photz_med	Median of the $P(z)$
18	photz_med_l68	Lower 68.3% confidence interval of photz_med
19	photz_med_u68	Upper 68.3% confidence interval of photz_med
20	specz	The spectroscopic redshift
21	specz_ref	The source of the spectroscopic redshift

Note. The `photz` column is the best redshift to use, and generally consists of the median of the $P(z)$ (i.e., `photz_med`). However, sometimes if the first peak is at low redshift ($z < 0.1$), it is instead the second $P(z)$ peak (i.e., `zpeak2`) to avoid issues with the photometric-redshift software as described in the text. Missing or irrelevant values are set to -99 .

inspect all sources with photometric-redshift outliers (defined as $|z_{\text{spec}} - z_{\text{phot}}| / (1 + z_{\text{spec}}) > 0.15$) and remove those with anomalous behavior affecting the input photometry. These are typically sources contaminated by very bright, extended sources not caught by the automated neighbor cut, but also include sources with other contaminants, including stars or diffraction spikes. The final visual vetting removes 0.5% of all available redshifts. After the vetting procedure, we compile a spectroscopic-redshift catalog including 8081 redshifts in total over the four CANDELS fields.

The spectroscopic redshifts from this compilation (limited to those available publicly) are included in the photometric-redshift catalog released as part of this work (see Section 5 and Table 2).

3.2. Combining Photometric Redshifts

In order to combine the results from the five individual runs into a single estimate for the photometric redshift, we add together the individual probability distribution functions, $P(z)$, following the procedure outlined in T. Dahlen et al. (2013; see their Section 5.2).

Before combining the individual $P(z)$, it is imperative to ensure that the photometric-redshift accuracy estimated from the individual codes is consistent and representative of the actual sample of galaxies for which the photometric redshifts are derived. One common check is to compare the 1σ uncertainty from the $P(z)$ with that derived directly from the offsets with respect to the spectroscopic reference sample (e.g., O. Ilbert et al. 2009). In the cases where the $P(z)$ underestimates (overestimates) the statistical errors from the spectroscopic sample comparison, a smoothing (sharpening) can be applied to the $P(z)$ to ensure that the error estimates on

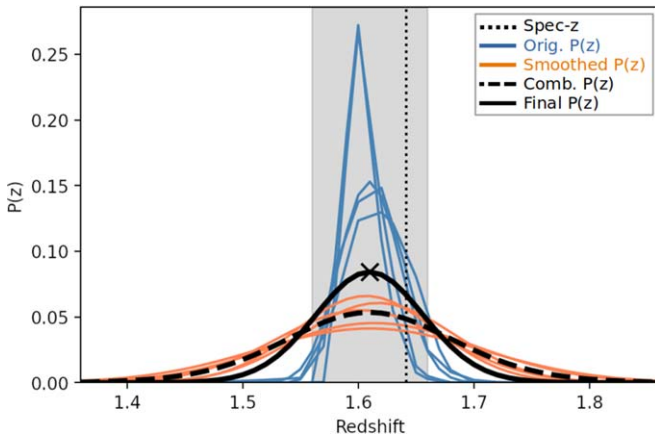


Figure 1. An example of the photometric-redshift probability distribution combination process for an example source (COSMOS-697: $z_{\text{spec}} = 1.6418$; $z_{\text{phot}} = 1.61 \pm 0.05$). Blue curves show the $P(z)$ s from the individual codes, orange curves show these $P(z)$ s after smoothing, and the black curves show the final combined $P(z)$ before (dashed) and after (solid) the final sharpening procedure. The final photometric redshift (cross symbol) and confidence intervals (shaded gray region) of the final $P(z)$ are shown, along with the spectroscopic redshift (dotted line).

the photometric redshifts are accurate and consistent (e.g., T. Dahlen et al. 2013).

Similar to T. Dahlen et al. (2013), we find that the individual codes used in our analysis underestimate their confidence intervals, i.e., fewer than 68.3% (1σ) of galaxies with known spectroscopic redshifts fall within their 68.3% confidence intervals from the photometric-redshift probability distributions $P(z)$. Hence, to alleviate this, we iteratively smooth each $P(z)_i$ for code i and redshift bin j by

$$P(z_j)_i = 0.25P(z_j - 1)_i + 0.5P(z_j)_i + 0.25P(z_j + 1)_i \quad (1)$$

until 68.3% of the known spectroscopic redshifts fall within the smoothed $P(z)$ 68.3% confidence intervals. We perform this smoothing procedure for each code separately, as each code requires a different number of smoothing iterations. Next, we add the smoothed probability distributions from each code together and renormalize. Similar to T. Dahlen et al. (2013), we find that after combining these resulting probability distributions, they tend to overestimate the confidence intervals, and hence we apply a sharpening according to $P(z_j)_i^{1/\alpha}$, where the exponent α is chosen to ensure 68.3% of the spectroscopic redshifts fall within the 68.3% confidence intervals. This results in a single $P(z)$ that combines the knowledge for all individual fitting codes with a corresponding error (or confidence interval) that is statistically consistent with the spectroscopic reference sample used for calibration. The final probability distributions are on a redshift grid of $z = 0-12$ in steps of 0.01. Figure 1 shows an example of this combination procedure for an individual source.

We note that when the photometric-redshift codes fail, they output a redshift of ~ 0 at high probability, which can affect the combined redshifts. For example, a failure mode of EAZY returns a redshift of ~ 0.01 with 100% confidence in the $P(z)$. This throws off the combined $P(z)$ distribution, resulting in a redshift at $z < 0.06$ due to the high confidence over a small redshift range. Since the number of expected galaxies at $z < 0.06$ in the field of view is extremely small, we truncated the redshift catalog at $z = 0.06$ to avoid cases with code failures.

Table 3
Column Descriptions for the Catalog Presenting the Photometric-redshift Probability Distribution $P(z)$

No.	Parameter	Description
1	field	The CANDELS field
2	id	The CANDELS ID
3	RA	R.A.
4	Dec	Decl.
5	pz	$P(z)$

Note. The third column consists of the photometric-redshift probability distribution $P(z)$ on a redshift grid from $z = 0-12$ in steps of 0.01. This probability function is useful when considering how robust a photometric redshift is.

We identify multiple peaks in each $P(z)$ as those with a peak and prominence at least 10% that of the main peaks, and with no higher peak within $0.06(1+z)$. The confidence intervals for each peak are calculated from the minimums between two neighboring peaks. We record up to three separate redshift peaks in the final photometric-redshift catalogs, sorted by height (z_{peak1} , z_{peak2} , z_{peak3}). Overall, we find that 20.5% of sources have two peaks, and 3.4% have three peaks. Typically, the final photometric redshift and its associated error is recorded as the median and 68.3% confidence intervals of the $P(z)$. However, for the $\sim 1\%$ of sources that have multiple peaks with the main peak at $z < 0.1$, we instead record the second peak as the final photometric redshift, as the main peak could be due to some codes failing to find a good fit.

The final photometric redshifts along with their errors are provided in the photometric-redshift catalog (see Table 2) and the full redshift probability distributions are also provided separately (see Table 3).

3.3. Quality of Resultant Redshifts

Figure 2 shows the comparison between the photometric redshifts and spectroscopic redshifts for each CANDELS field, as well as the overall scatter (normalized median absolute deviation, NMAD) defined by

$$\sigma_{\text{NMAD}} = 1.48 \times \text{median}(|\Delta z|/(1 + z_{\text{spec}})) \quad (2)$$

and outlier fraction η , where

$$\eta = |\Delta z|/(1 + z_{\text{spec}}) > 0.15. \quad (3)$$

Figure 2 shows the performance in each individual field. We find that η is lower for fields with more filters (e.g., COSMOS has the lowest η). On the other hand, we see the best σ_{NMAD} for GOODS-N and GOODS-S, which have the most filters and deepest imaging. Overall, EGS performs the worst with the fewest filters, but still has relatively low η and σ_{NMAD} given the excellent coverage.

The top-left panel of Figure 3 shows the performance on the combined sample across all fields. We obtain an average σ_{NMAD} of 0.0263 and outlier fraction η of 1.32%. This is within family of the other photometric redshifts determined for the CANDELS fields (e.g., T. Dahlen et al. 2013; R. E. Skelton et al. 2014; R. Bezanson et al. 2016; D. Kodra et al. 2023). We note that the quality of σ_{NMAD} and η depends on the quality of the spectroscopic sample being compared to. Therefore, it is not useful to carefully compare the values of σ_{NMAD} and η between studies of the same fields determined from different

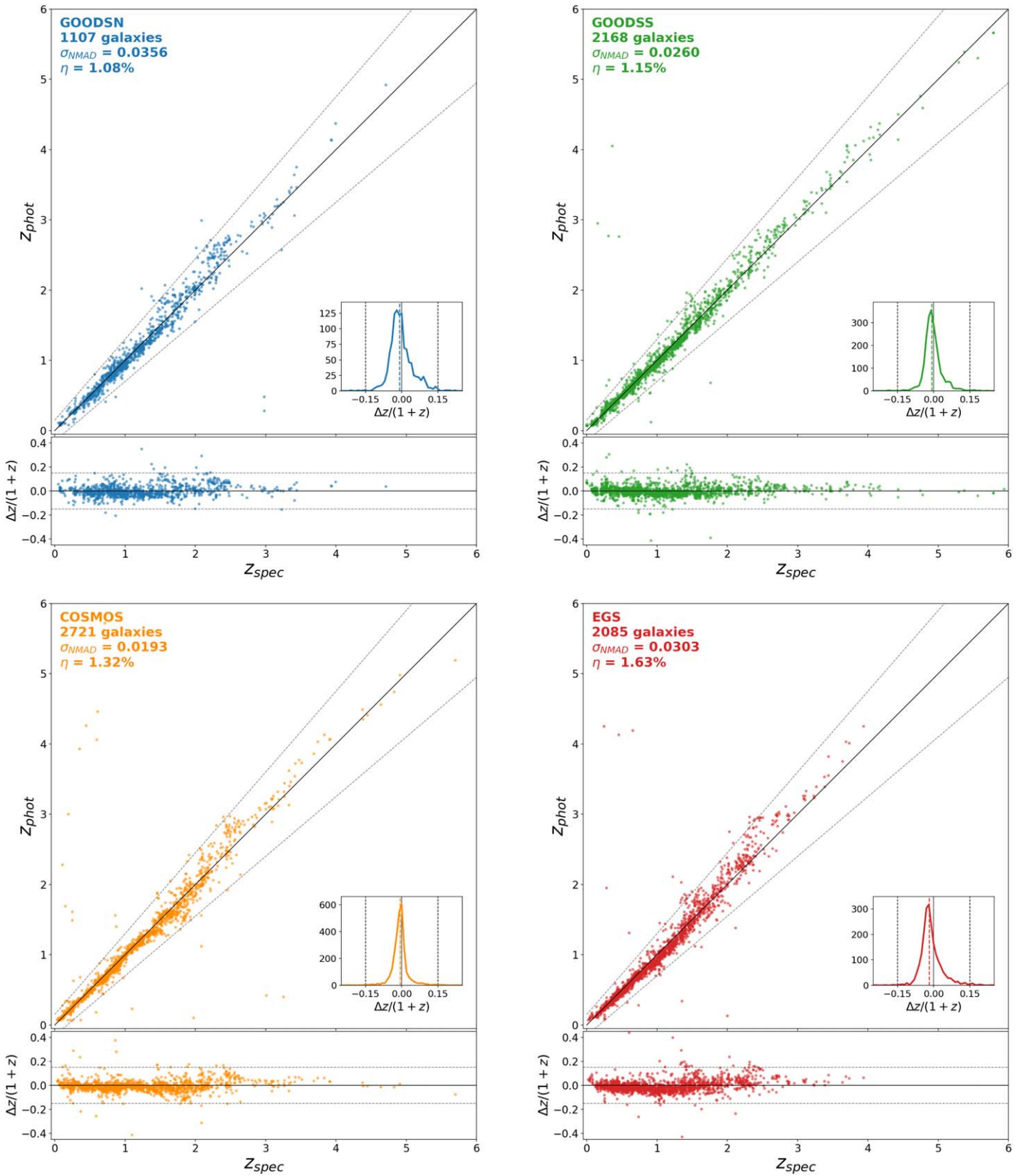


Figure 2. Comparison of the performance of the photometric redshifts with the spectroscopic sample for each of the individual fields. The key statistics, i.e., the scatter (σ_{NMAD}) and the outlier fraction ($\eta = |\Delta z|/(1+z) > 0.15$) are reported in the upper left corner. The inset shows the distribution of the fractional differences between the photometric and spectroscopic redshifts. The dotted lines show the outlier criterion: $z_{\text{phot}} = z_{\text{spec}} \pm 0.15(1 + z_{\text{spec}})$ and the dashed lines show the median of the distribution.

spectroscopic samples. In fact, we could probably improve our η further by careful inspection of all the spectroscopic data, but that is out of the scope of this paper. On the other hand, we can

investigate the improvements in photometric redshifts with the addition of the UVCANDELS data with the same spectroscopic sample.

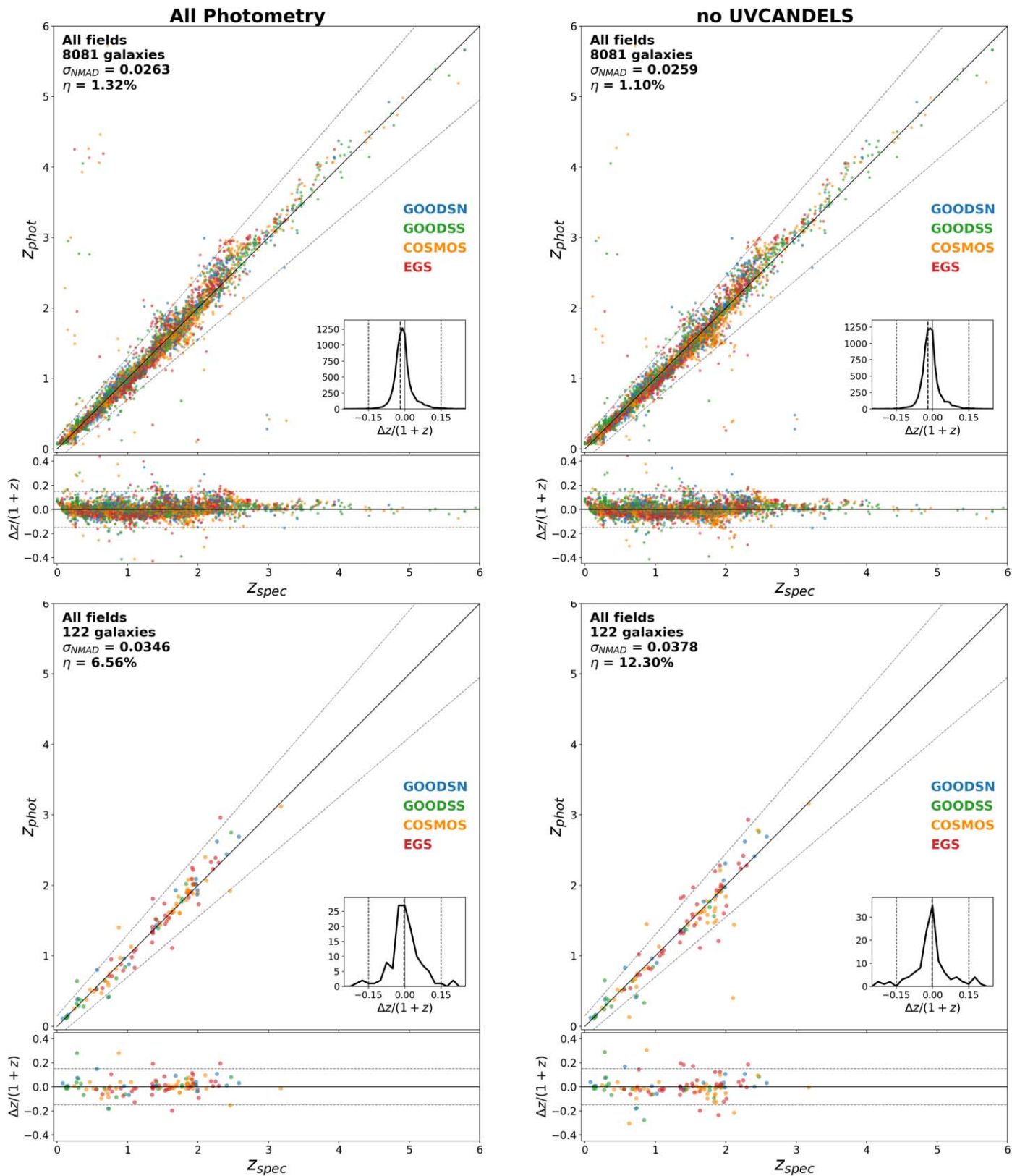


Figure 3. An aggregate comparison between the photometric and spectroscopic redshifts for all four CANDELS fields combined. The left panels show the comparison where all available filters were included in the photometric-redshift fitting, where as the right panels show the same without using filters from the UVCANDELS program (i.e., F275W/F435W for COSMOS and EGS; F275W for GOODS-N and GOODS-S). The top panels include all sources, where as the bottom panels only show sources with multiple peaks in their probability distributions $P(z)$ and with $SNR > 3$ in F275W. The improvement of the photometric redshift by including the UV photometry is evident in this case, reducing both σ_{NMAD} and η for sources detected in the UV or that previously had multiple peaks in $P(z)$.

3.4. Improvement of Photometric Redshifts with UVCANDELS Data

Aside from the fiducial case (all photometry), in order to quantify the impact of including the new UV photometry from UVCANDELS we repeat the analysis of estimating photometric redshifts for an additional scenario without including the UVCANDELS photometry, i.e., no F275W for all fields and no F435W for COSMOS and EGS. The results from this test are shown in Figure 3.

As evident from Figure 3, high-fidelity photometric-redshift estimates can be obtained with and without the inclusion of UVCANDELS photometry (i.e., F275W/F435W); the scatter and outlier fraction are within 0.004% and 0.22%, respectively. This is because the vast majority of galaxies in the catalogs do not have detections in the UV, either because they are too faint, or because they are at high redshift. Unlike in the UVUDF where the UV limits significantly improved the photometric redshifts (M. Rafelski et al. 2015), the depth of the UVCANDELS data only provide modest limits for nondetections, which do not significantly help the redshift determinations which already are based on many filters. Additionally, these fields have ground-based u -band data as well, already providing useful limits on nondetections at similar wavelengths, and further reducing the benefits of the F275W and F435W from UVCANDELS for photometric redshifts.

For a more useful measure of the improvement provided by the UV data to the photometric redshifts, we limit ourselves to sources with significant F275W fluxes. The bottom row in Figure 3 shows only those sources with multiple $P(z)$ peaks and $\text{SNR} > 3$ in F275W. In this case, the improvement in the photometric-redshift quality when including UV data is significantly more evident; the scatter and outlier fraction fall by 0.003% and 5.7%, respectively. The percentage of sources with multiple peaks also decreases from 23.4% to 20.5% after including the UV data.

4. Galaxy Physical Properties

The SFH represents one of the core components for defining a stellar population for a galaxy and consequently, its SED. Traditionally, galaxy SED-modeling tools have typically implemented fixed, functional forms to parameterize galaxy SFHs, such as exponentially rising/declining, delayed exponential, constant, short bursts, or some linear combination thereof. However, modern SED-modeling tools have evolved beyond the basic functional forms to now allow for more flexible, and even nonparametric forms for the galaxy SFH. Several recent studies have investigated the differences in the stellar physical parameters estimated from parametric and nonparametric approaches (e.g., S. Lower et al. 2020; C. Pacifici et al. 2023; S. Jain et al. 2024; Y. Kaushal et al. 2024) and the general consensus from comparisons of observations to simulations is a preference for the nonparametric or flexible-SFH approach, which returns more accurate physical parameters (e.g., K. Iyer & E. Gawiser 2017; K. G. Iyer et al. 2019; J. Leja et al. 2019).

With the rich UVCANDELS+CANDELS multiwavelength photometric data set and redshifts described in Sections 2.2 and 3, respectively, here we investigate the impact of the SFH parameterization on the inferred galaxy physical properties from the observational perspective. In this work, we implement two parallel approaches for modeling galaxy SEDs and

estimating galaxy physical parameters: (i) a modern approach that facilitates flexible SFHs, and (ii) a fiducial approach that utilizes traditional, fixed, functional SFHs. In the following sections, we describe our methodology for each of these approaches. For both, we use the photometric data set described in Section 2.2 for the SED modeling.

4.1. Fitting Flexible SFHs with DENSE BASIS

For the flexible-SFH approach, we use the SED-modeling tool DENSE BASIS³⁹ (K. G. Iyer et al. 2019), which uses Gaussian process (GP) regression to model highly flexible SFHs. The key advantage of the GP-based formalism is its ability to encode the maximum amount of information in the complex galaxy SFHs using a minimal number of parameters. As demonstrated in K. G. Iyer et al. (2019), this formalism minimizes the bias in estimating galaxy SFHs at all look-back times, compared to the parametric (functional) approaches.

4.1.1. Defining the SFHs

The galaxy SFHs in DENSE BASIS are described using a fixed number of “shape” parameters (N). These shape parameters (t_X) are N look-back times at which the galaxy formed equally spaced quantiles of its total mass (see K. G. Iyer et al. 2019 for a more detailed description). For this work, we adopt $N = 4$ shape parameters for describing the galaxy SFHs with four t_X parameters: t_{20} , t_{40} , t_{60} , and t_{80} , representing the look-back times⁴⁰ at which the galaxy assembled 20%, 40%, 60%, and 80% of its total stellar mass, respectively. We choose $N = 4$ for the GP-based SFH parameterization as it allows for sufficient flexibility (K. G. Iyer et al. 2019) while minimizing the computation time for the SED modeling.

Furthermore, we allow the GP-based SFHs to have a “decoupled” star formation episode over the most recent 100 Myr, which still retains continuity with the rest of the SFH but allows for further flexibility in fitting any recent star formation traced by the newly added rest-frame UV data from UVCANDELS.

4.1.2. Galaxy Model Template Library

The galaxy model templates in DENSE BASIS are defined using the Flexible Stellar Population Synthesis⁴¹ (FSPS; C. Conroy et al. 2009; C. Conroy & J. E. Gunn 2010a) library, which includes a self-consistent prescription for both the stellar continuum as well as nebular emission. The nebular emission lines and continuum implementation in FSPS is based on the CLOUDY models from N. Byler et al. (2017). We also use the built-in B. T. Draine & A. Li (2007) model for dust emission.

For this analysis, we assume a G. Chabrier (2003) initial mass function (IMF), which is a well-established choice when fitting the SEDs of a general galaxy population, particularly at higher redshifts where galaxies tend to be relatively more star-forming and have lower metallicities (see e.g., G. Chabrier et al. 2014; A. M. Hopkins 2018). We adopt the P. Madau (1995) model for IGM absorption, and the D. Calzetti et al. (2000) dust-attenuation law, which couples the attenuation for young and older stars (i.e., assumes the same dust attenuation

³⁹ <https://dense-basis.readthedocs.io/en/latest/>, <https://dfm.io/python-fsps/>

⁴⁰ These look-back times are defined as the fraction of the age of the Universe (at the given redshift for a galaxy).

⁴¹ <https://github.com/cconroy20/fsps>

Table 4

Column Descriptions for the Catalog Presenting the Galaxy Physical Properties Computed from DENSE BASIS

No.	Parameter	Description
1	ID ^a	Identification number
2	RA	R.A.
3	Dec	Decl.
4	photz	Photometric redshift used (from Table 2)
5	delz	Error on photometric redshift (assumed)
6	nbands	Number of photometric bands used for fitting
Parameter Estimates from the Posterior Distribution		
7–9	logM ^b	Galaxy stellar mass estimate [log M_{\odot}]
10–12	logSFR ^b	Star formation rate [log $M_{\odot} \text{ yr}^{-1}$]
13–15	Av ^b	Dust attenuation (V band) [mag]
16–18	logZsol ^b	Stellar metallicity [log Z_{\odot}]
19–21	t20 ^b	Time ^c when 20% of galaxy mass was formed
22–24	t40 ^b	Time ^c when 40% of galaxy mass was formed
25–27	t60 ^b	Time ^c when 60% of galaxy mass was formed
28–30	t80 ^b	Time ^c when 80% of galaxy mass was formed
31–33	color_nuvu ^b	Rest-frame NUV – U color
34–36	color_nuvr ^b	Rest-frame NUV – R color
37–39	color_uv ^b	Rest-frame U – V color
40–42	color_vj ^b	Rest-frame V – J color
43–45	color_rj ^b	Rest-frame R – J color
46	flags	Quality flags ^d
Parameter Estimates from the Minimum- χ^2 Model		
47	logM_chi2	Galaxy stellar mass estimate [log M_{\odot}]
48	logSFR_chi2	Star formation rate [log $M_{\odot} \text{ yr}^{-1}$]
49	Av_chi2	Dust attenuation (V band) [mag]
50	logZsol_chi2	Stellar metallicity [log Z_{\odot}]
51	t20_chi2	Time ^c when 20% of galaxy mass was formed
52	t40_chi2	Time ^c when 40% of galaxy mass was formed
53	t60_chi2	Time ^c when 60% of galaxy mass was formed
54	t80_chi2	Time ^c when 80% of galaxy mass was formed
55	color_nuvu_chi2	Rest-frame NUV – U color
56	color_nuvr_chi2	Rest-frame NUV – R color
57	color_uv_chi2	Rest-frame U – V color
58	color_vj_chi2	Rest-frame V – J color
59	color_rj_chi2	Rest-frame R – J color
60	chi2	χ^2 value for the minimum- χ^2 solution
Model Magnitudes from the Best-fit Template ^e		
61–69	model_Lnu_rest [*]	Model template fluxes for rest-frame Johnson filters (FUV, NUV, <i>UBVRJK</i>) [μJy]
70–	model_Fnu_ [*] f	Model template fluxes for observed photometric bands [μJy]

Notes.

^a The galaxy ID number is consistent with that from the CANDELS photometric catalogs and the catalogs for each field are provided separately.

^b For these columns, each has two additional columns named *_16 and *_84 denoting the 1σ (68%) confidence interval for the best estimate.

^c The time is given as the fraction of the age of the Universe (at the redshift of the galaxy).

^d Quality flags: 1 = invalid fit (nan for mass estimate); 2 = large SFR uncertainties ($\Delta(\log \text{SFR}) > 2$); 3 = objects flagged as stars in photometry catalog (CLASS_STAR > 0.5); 4 = poor fit/large χ^2 (> 1000).

^e These model magnitudes are computed for the best-fit parameters estimated from the full Bayesian posterior distribution (not the minimum- χ^2 solution).

^f The model magnitudes are available for the specific set of photometric bands included in the SED modeling, which differs from field to field.

for the nebular and stellar components) with one free parameter: A_V , the V-band dust attenuation. We also assume the gas-phase metallicity to be equal to the stellar metallicity

(left as a free parameter), and the ionization parameter for the nebular gas is left as default ($\log U = -2$).

The template redshifts are set to the galaxy’s photometric redshifts defined in Section 3. During fitting, a nominal error of $\delta(z) = 0.025 \cdot z/(1+z)$ is assumed to ensure a robust estimation for the galaxy physical parameters.

4.1.3. Priors and Parameter Estimation

Ultimately, we perform the fitting with eight free parameters: the galaxy stellar mass (M^*), star formation rate (SFR; over the recent 100 Myr), the stellar dust attenuation (A_V), the stellar metallicity (Z^*), and the four t_X parameters ($t_{20}, t_{40}, t_{60}, t_{80}$) that define the galaxy SFH.

We jointly define the prior for M^* and SFR as the specific star formation rate (sSFR = SFR/ M^*), which is assumed as a uniform (flat) prior spanning a range of $\log(\text{sSFR}) = -12$ to -7 yr^{-1} . We adopt uniform (flat) prior for A_V spanning from $A_V = 0$ to 4, and for Z^* over $\log(Z/Z_{\odot}) = -1.5$ –0.25. For the GP-based SFH parameters, i.e., the t_X look-back times, we adopt a Dirichlet prior with $\alpha = 5$ as per the recommendation from K. G. Iyer et al. (2019), which leads to a distribution of parameters that is well matched to galaxies in simulations.

We perform parameter estimation for DENSE BASIS in two ways: (i) For each galaxy, a likelihood is computed from the sufficiently large number of model SEDs realized in the pregenerated grid library with parameters drawn according to the priors described above. This results in a posterior distribution for each of the free parameters. The posterior medians and 1σ (68%) percentiles are then used to define the best-fit parameters and the associated errors. (ii) A simpler, frequentist approach is also implemented that uses the (single) SED from the pregenerated library with the minimum χ^2 value to define the best-fit parameters, with no uncertainties reported.

The estimates from the full posterior analysis are generally more robust and preferred over the simple minimum χ^2 result, but we provide both for completeness and as a consistency check (see Table 4). Figure 4 demonstrates the modeling for an example galaxy along with the full posterior distributions for the free parameters. The full mass–redshift distribution for each of the fields is shown in Figure 5.

4.2. Fitting Fixed SFHs with CIGALE

For our fiducial approach, we use the traditional approach of using fixed, functional forms for the galaxy SFHs. In this case, we implement the Code Investigating GALaxy Emission⁴² (CIGALE; D. Burgarella et al. 2005; S. Noll et al. 2009; M. Boquien et al. 2019) tool for the estimation of the galaxy physical properties.

4.2.1. Defining the SFHs

For the galaxy SFH parameterization within CIGALE, we adopt a delayed-exponential functional form⁴³ with an additional possibility for an episode of recent starburst (similar as with DENSE BASIS) with an exponentially declining functional form. The SFH is parameterized with an overall age (t_{age}) and an e -folding timescale (τ) for the main stellar population, along with an age (t_{burst}) and an e -folding timescale

⁴² <https://cigale.lam.fr/>

⁴³ $\text{SFR}(t) \propto t e^{-t/\tau}$.

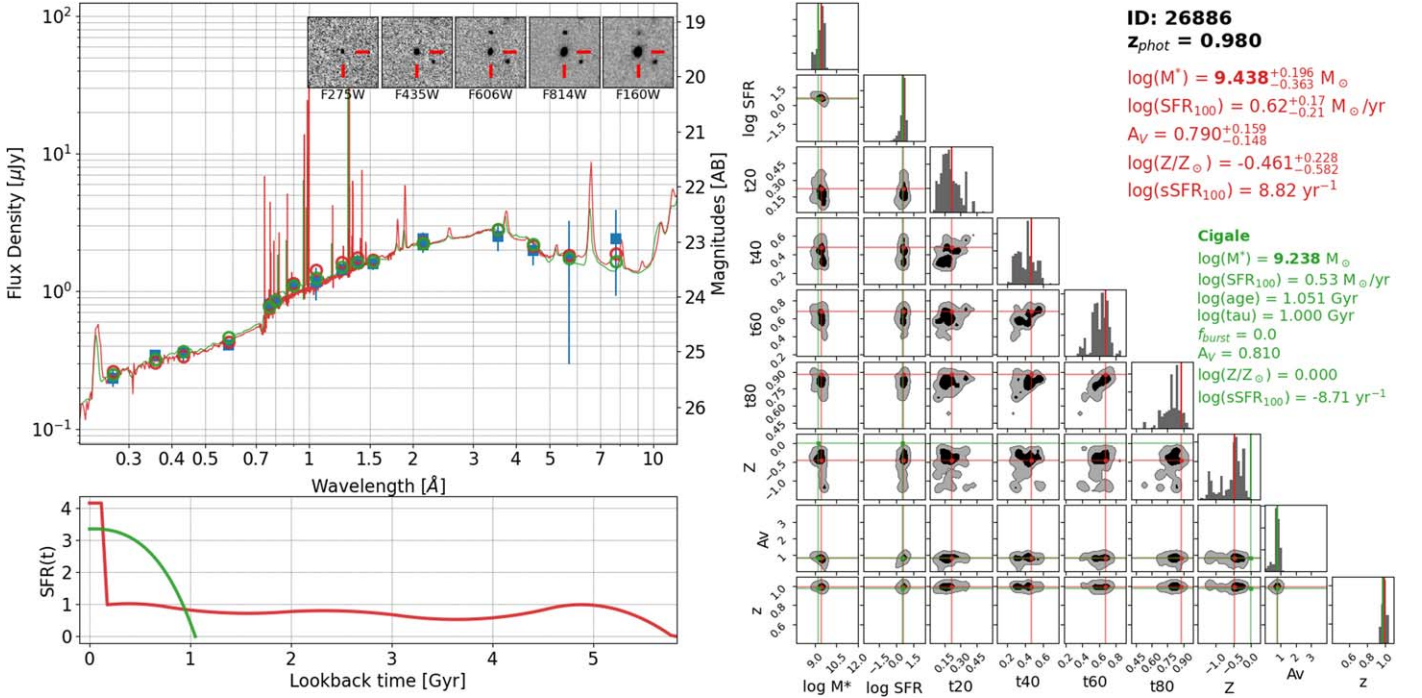


Figure 4. The SED modeling shown for an example galaxy (GOODS-N-26886). The top-left panel shows the observed photometry (shown in blue) along with the best-fit model template from the flexible (DENSE BASIS, in red) and fixed (CIGALE, in green) SFH assumptions. The insets show $5'' \times 5''$ postage stamps of the galaxy in the respective filters. The bottom-left panel shows the best-fit SFH for both cases demonstrating how the flexible-form SFH captures star formation at earlier times that is missed by the fixed-form approach, while both return an excellent overall fit to the observed photometry. For the DENSE BASIS result, a corner plot with the posterior distributions of the free parameters is shown on the right along with the best-fit parameter values for both cases.

(τ_{burst}) for the burst episode as well as the fraction of mass formed in the burst phase (f_{burst}).

In order to keep the computational times manageable, we fix the burst population’s t_{burst} and τ_{burst} parameters to 10 Myr and 50 Myr, respectively, while the remaining parameters (t_{age} , τ_{age} , and f_{burst}) are varied freely.

4.2.2. Galaxy Model Template Library

Here, we use the G. Bruzual & S. Charlot (2003) stellar population models, along with the prescription for nebular emission (both emission line and continuum) included within CIGALE, which is based on A. K. Inoue (2011). We note that the IGM prescriptions between CIGALE and DENSE BASIS (Section 4.1) are not identical, which is a technical limitation as these are the only prescriptions available within the respective codes. We use the dust-emission model from D. A. Dale et al. (2014) included in CIGALE.

For this analysis, we assume a G. Chabrier (2003) IMF and that the prescription from A. Meiksin (2006) is used for the IGM absorption. Similar to the flexible-SFH case, we adopt the D. Calzetti et al. (2000) dust law (which assumes the same attenuation for young and older stars (and hence the nebular and stellar dust components)) parameterized by the free parameter A_V or $E(B - V) = A_V/4.05$. Here, the gas-phase metallicity is assumed to be solar and the gas ionization parameter is left at its default value ($\log U = -2$).

The template redshifts are set to the galaxy’s photometric redshifts defined in Section 3. In the case of CIGALE, since all models are generated at the input redshifts, the galaxy redshifts are treated as exact, albeit rounded to two decimals to manage computation time.

4.2.3. Parameter Estimation

For this CIGALE implementation, we have seven free parameters: the galaxy stellar mass (M^*), star formation rate (SFR), stellar dust attenuation (A_V), stellar metallicity (Z^*), and the SFH-related parameters of t_{age} , τ_{age} , and f_{burst} .

For the main stellar population in the SFH, the age, t_{age} , is allowed to vary over a grid of 21 points from 10 Myr to the age of the Universe and similarly τ_{age} is varied freely over a grid spanning over 30 Myr to 30 Gyr. For the burst component, f_{burst} is allowed to vary (over gridded values from 0 to 1). Lastly, the dust-attenuation parameter $E(B - V) = A_V/4.05$ is varied over $[0, 1.2]$ and the stellar metallicity over $\log(Z/Z_\odot) = [-2.3, 0.4]$.

The best-fit parameters are estimated by performing a minimum χ^2 search over a template library generated from the full grid of free parameters. As part of the output, an instantaneous as well as a 100 Myr averaged SFR is reported (see Table 5). The resulting best-fit solutions from both the flexible (DENSE BASIS) and fixed (CIGALE) approaches for an example galaxy is shown in Figure 4 while the full mass-redshift distribution for each field is shown in Figure 5.

4.3. The Impact of the SFH Assumption on Parameter Estimates

From a statistical perspective, the SED modeling with either of the approaches (flexible/DENSE BASIS or fixed/CIGALE) is relatively robust with no significant systematic biases in the fitting residuals. As illustrated in Figure 4 with an example galaxy, the best-fit model template from both methodologies represents a qualitatively good fit to the observed photometry.

However, a population comparison of the best-fit parameters reveals significant systematic biases in even the most basic

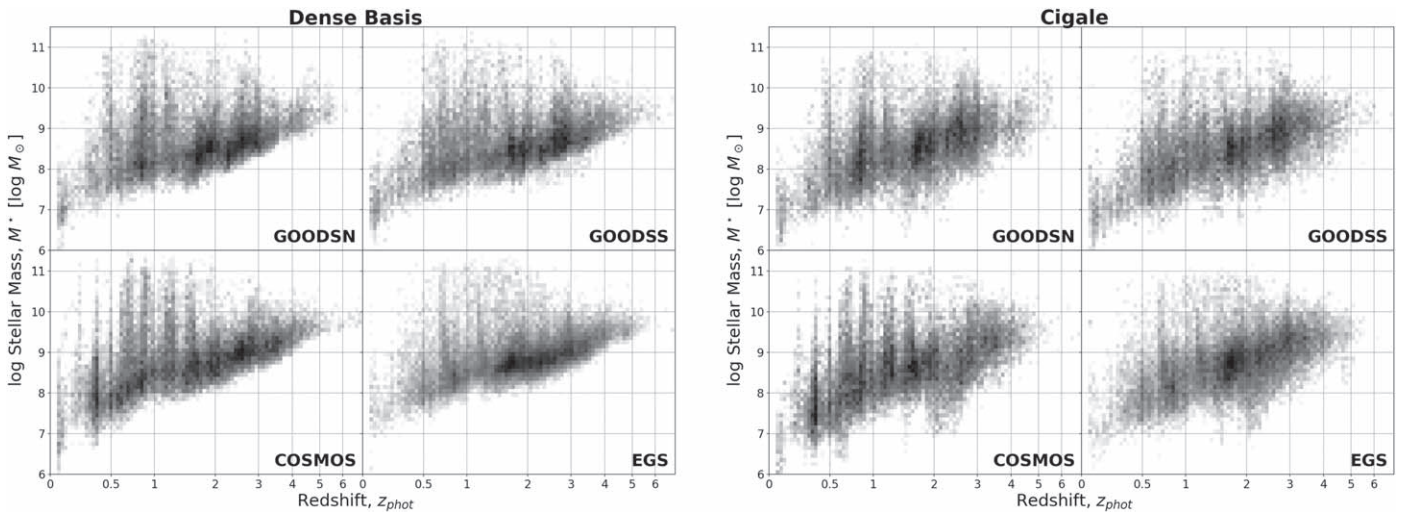


Figure 5. The mass distribution as a function of redshift for each field, with the masses estimated using the flexible (DENSE BASIS, left panel) and fixed (CIGALE, right panel) SFH assumptions.

physical property, the galaxy stellar mass. Figure 6 shows the difference in the stellar mass inferred from the two approaches and it is evident that the masses estimated from the flexible-SFH assumption (DENSE BASIS) are systematically higher, particularly at the low-mass end. For typical galaxies ($\sim 10^9\text{--}10^{10} M_{\odot}$), the stellar masses are in good agreement regardless of the SFH parameterization. However, below $\sim 10^9 M_{\odot}$, the flexible-SFH stellar masses get increasingly biased by as much as 0.5 dex at $\sim 10^7 M_{\odot}$. Similarly, at the high-mass end ($\gtrsim 10^{10} M_{\odot}$), the masses from DENSE BASIS are also systematically higher, albeit only by ~ 0.2 dex.

This discrepancy in the estimated stellar masses due to different SFH assumptions is not new and has already been reported in the literature (e.g., J. Leja et al. 2019; S. Lower et al. 2020; S. Jain et al. 2024). Our results here are broadly consistent with the previous findings. From comparisons to simulated galaxies, it is clear that the stellar masses estimated using flexible SFHs are closer to the true value and it is the fixed-form SFHs that underestimate the stellar masses (e.g., S. Lower et al. 2020). This is due to their inability to simultaneously capture the multiple episodes of star formation and other gradual changes in the SFHs. This effect is also evident in the example shown in Figure 4, where the fixed SFH (from CIGALE; in green) is missing the early episode of star formation captured by the flexible SFH (from DENSE BASIS; in black). This effect is amplified particularly at the lower-mass end ($\lesssim 10^9 M_{\odot}$) where galaxies tend to have more chaotic, bursty SFHs with multiple episodes of prominent star formation activity, which can contribute relatively large differences in their galaxies’ stellar masses (e.g., N. Emami et al. 2019). On a similar note, at higher masses, it is likely that the functional form of the fixed SFHs is missing the extended periods of star formation activity due to the choice of parameterization, again resulting in underestimated masses.

5. Catalog Descriptions

From the analysis presented here, we produce catalogs listing new photometric redshifts as well as galaxy physical properties for the four CANDELS fields covered by UVCANDELS (GOODS-N, GOODS-S, COSMOS, EGS). These catalogs will be publicly

Table 5

Column Descriptions for the Catalog Presenting the Galaxy Physical Properties Computed from CIGALE

No.	Parameter	Description
1	ID	Identification number
2	RA	R.A.
3	Dec	Decl.
4	photz	Photometric redshift used (from Table 2)
5	logM	Galaxy stellar mass [$\log M_{\odot}$]
6	logSFR	Instantaneous star formation rate [$\log M_{\odot} \text{ yr}^{-1}$]
7	logSFR100	100 Myr averaged star formation rate [$\log M_{\odot} \text{ yr}^{-1}$]
8	Av	Dust attenuation (V band) [mag]
9	logZsol	Stellar metallicity [$\log Z_{\odot}$]
10	logage	Age of the main stellar population [$\log \text{ yr}$]
11	logtau	e -folding timescale of the main stellar population [$\log \text{ yr}$]
12	f_burst	Fraction of mass formed in the late burst ^a
13	color_fuvnuv	Rest-frame FUV – NUV color
14	color_nuvr	Rest-frame NUV – R color
15	chi2	Reduced χ^2 value
16–	model_Fnu_*	Model template fluxes for observed photometric bands [μJy]

Note.

^a The late burst is characterized as a (fixed) 10 Myr old exponentially declining episode of star formation with an e -folding timescale of 50 Myr.

released via MAST at doi:[10.17909/8s31-f778](https://doi.org/10.17909/8s31-f778). The full output is delivered with the following catalogs:

1. a catalog presenting the photometric redshifts from Section 3 (see column description in Table 2);
2. the full probability distribution, $P(z)$, for the photometric redshifts from Section 3 (see column description in Table 3);
3. catalogs for each field listing the best-fit galaxy physical properties estimated using DENSE BASIS with the flexible-SFH assumption from Section 4.1 (see column description in Table 4); and
4. per-field galaxy physical property catalogs from CIGALE (fixed SFH assumption) from Section 4.2 (see column description in Table 5).

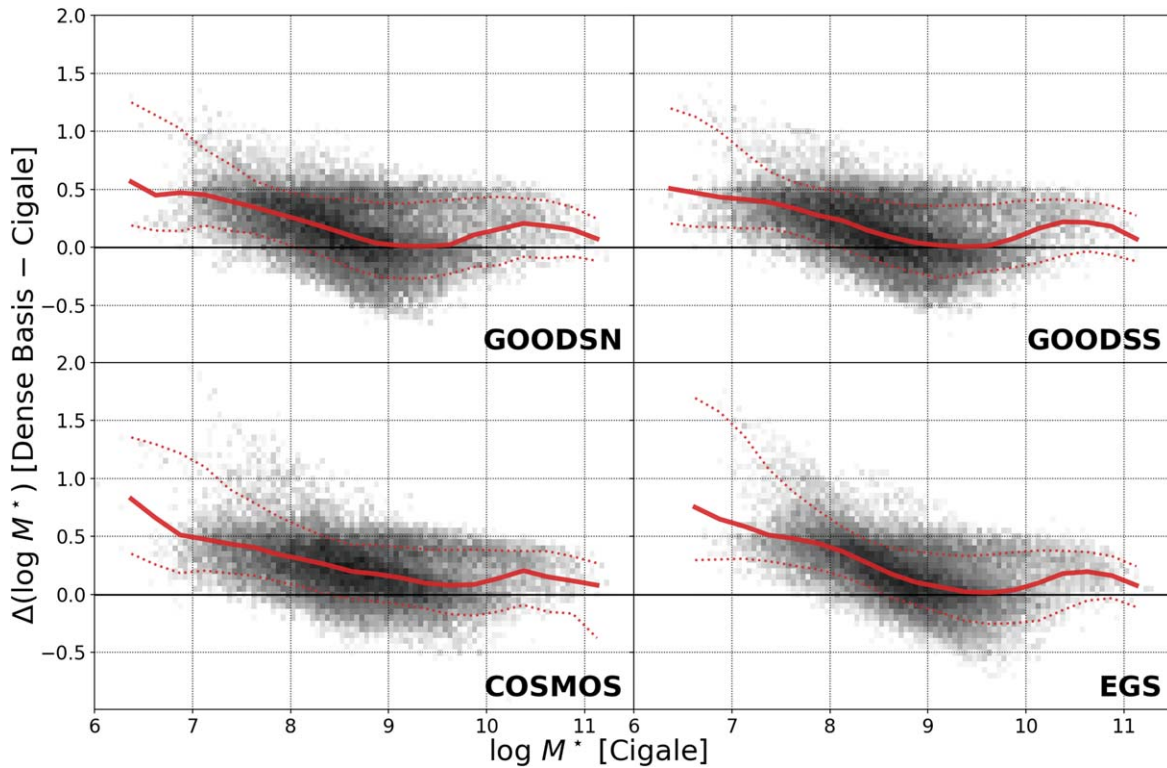


Figure 6. The difference between the galaxy stellar masses estimated from flexible (DENSE BASIS) and fixed (CIGALE) SFH approaches. The red curves show the running median (solid) and the 68% (1σ) percentile for the population. Even when fitting the same photometric data set with consistent assumptions, the inferred stellar masses are significantly impacted by the parameterization of the galaxy SFH during SED modeling.

6. Summary

We present a set of new measurements for photometric redshifts and galaxy physical parameters for over 150,000 galaxies in four of the five CANDELS fields (GOODS-N, GOODS-S, COSMOS, EGS; combined area of ~ 430 arcmin²) covered by the recent Hubble Treasury program, UVCANDELS. In this work, we utilize the UV-to-IR photometric data set available for these fields from a combination of the existing HST optical/NIR, Spitzer mid-IR, and other ancillary ground-based imaging as well as the newly acquired WFC3/UVIS F275W and ACS/WFC F435W (for COSMOS and EGS) imaging from UVCANDELS, to model the galaxy SEDs using state-of-the-art fitting tools.

Our key findings are as follows:

1. The inclusion of UV photometry significantly improves the photometric redshift for sources with significant UV detections and degenerate redshift solutions. After adding UV photometry when measuring the redshifts, we find significantly lower outlier fractions for sources with $\text{SNR} > 3$ in F275W and multiple peaks in their probability distributions, $P(z)$.
2. When modeling galaxy SEDs, the typical assumption of a fixed, functional form for the galaxy SFH systematically biases the measurement of even the most basic physical parameter—the galaxy stellar mass—at both the low-mass ($\lesssim 10^9 M_\odot$) and the high-mass ($\gtrsim 10^{10} M_\odot$) ends. We find the fixed-form SFHs to underestimate the stellar mass by as much as ~ 0.5 dex at $10^7 M_\odot$ and ~ 0.2 at $10^{10.5} M_\odot$.
3. This underestimation for the stellar mass is mainly driven by the inability of the fixed-form SFHs to simultaneously

capture the major star formation episodes as well as the prolonged lower-level star formation and/or other gradual changes in the galaxy SFHs.

The final catalogs presenting the photometric redshifts and physical parameters will be publicly available via the MAST archive at doi:[10.17909/8s31-f778](https://doi.org/10.17909/8s31-f778).


Acknowledgments

We thank the anonymous referee for their constructive feedback which helped improve the quality of the manuscript. The analysis presented in this paper is based on observations with the NASA/ESA Hubble Space Telescope obtained at the Space Telescope Science Institute, which is operated by the Association of Universities for Research in Astronomy, Incorporated, under NASA contract NAS5-26555. Support for Program Number HST-GO-15647 was provided through a grant from the STScI under NASA contract NAS5-26555. V. M., H.T., and X.W. acknowledge work carried out, in part, by IPAC at the California Institute of Technology, as was sponsored by the National Aeronautics and Space Administration.

Software: NumPy (C. R. Harris et al. 2020); SciPy (P. Virtanen et al. 2020); AstroPy (Astropy Collaboration et al. 2013, 2018, 2022); Matplotlib (J. D. Hunter 2007); FSPS (C. Conroy & J. E. Gunn 2010b); DENSE BASIS (K. G. Iyer et al. 2019); CIGALE (M. Boquien et al. 2019); EAZY (G. B. Brammer et al. 2008); BPZ (N. Benítez 2000; N. Benítez et al. 2004; D. Coe et al. 2006); LEPHARE (S. Arnouts et al. 1999; O. Ilbert et al. 2006); ZPHOT (E. Giallongo et al. 1998; A. Fontana et al. 2000).

ORCID iDs

Vihang Mehta  <https://orcid.org/0000-0001-7166-6035>
 Marc Rafelski  <https://orcid.org/0000-0002-9946-4731>
 Ben Sunnquist  <https://orcid.org/0000-0003-3759-8707>
 Harry I. Teplitz  <https://orcid.org/0000-0002-7064-5424>
 Claudia Scarlata  <https://orcid.org/0000-0002-9136-8876>
 Xin Wang  <https://orcid.org/0000-0002-9373-3865>
 Adriano Fontana  <https://orcid.org/0000-0003-3820-2823>
 Nimish P. Hathi  <https://orcid.org/0000-0001-6145-5090>
 Kartheik G. Iyer  <https://orcid.org/0000-0001-9298-3523>
 Anahita Alavi  <https://orcid.org/0000-0002-8630-6435>
 James Colbert  <https://orcid.org/0000-0001-6482-3020>
 Norman Grogin  <https://orcid.org/0000-0001-9440-8872>
 Anton Koekemoer  <https://orcid.org/0000-0002-6610-2048>
 Kalina V. Nedkova  <https://orcid.org/0000-0001-5294-8002>
 Matthew Hayes  <https://orcid.org/0000-0001-8587-218X>
 Laura Prichard  <https://orcid.org/0000-0002-0604-654X>
 Brian Siana  <https://orcid.org/0000-0002-4935-9511>
 Brent M. Smith  <https://orcid.org/0000-0002-0648-1699>
 Rogier Windhorst  <https://orcid.org/0000-0001-8156-6281>
 Teresa Ashcraft  <https://orcid.org/0000-0003-4439-6003>
 Micaela Bagley  <https://orcid.org/0000-0002-9921-9218>
 Ivano Baronchelli  <https://orcid.org/0000-0003-0556-2929>
 Guillermo Barro  <https://orcid.org/0000-0001-6813-875X>
 Alex Blanche  <https://orcid.org/0000-0003-2102-3933>
 Adam Broussard  <https://orcid.org/0000-0002-7767-5044>
 Timothy Carleton  <https://orcid.org/0000-0001-6650-2853>
 Nima Chartab  <https://orcid.org/0000-0003-3691-937X>
 Alex Codoreanu  <https://orcid.org/0000-0001-9560-9174>
 Seth Cohen  <https://orcid.org/0000-0003-3329-1337>
 Christopher Conselice  <https://orcid.org/0000-0003-1949-7638>
 Y. Sophia Dai  <https://orcid.org/0000-0002-7928-416X>
 Behnam Darvish  <https://orcid.org/0000-0003-4919-9017>
 Romeel Davé  <https://orcid.org/0000-0003-2842-9434>
 Laura DeGroot  <https://orcid.org/0000-0001-9022-665X>
 Duilia De Mello  <https://orcid.org/0000-0003-1624-8425>
 Mark Dickinson  <https://orcid.org/0000-0001-5414-5131>
 Najmeh Emami  <https://orcid.org/0000-0003-2047-1689>
 Henry Ferguson  <https://orcid.org/0000-0001-7113-2738>
 Leonardo Ferreira  <https://orcid.org/0000-0002-8919-079X>
 Keely Finkelstein  <https://orcid.org/0000-0003-0792-5877>
 Steven Finkelstein  <https://orcid.org/0000-0001-8519-1130>
 Jonathan P. Gardner  <https://orcid.org/0000-0003-2098-9568>
 Eric Gawiser  <https://orcid.org/0000-0003-1530-8713>
 Timothy Gburek  <https://orcid.org/0000-0002-7732-9205>
 Mauro Giavalisco  <https://orcid.org/0000-0002-7831-8751>
 Andrea Grazian  <https://orcid.org/0000-0002-5688-0663>
 Caryl Gronwall  <https://orcid.org/0000-0001-6842-2371>
 Yicheng Guo  <https://orcid.org/0000-0003-2775-2002>
 Pablo Arrabal Haro  <https://orcid.org/0000-0002-7959-8783>
 Shoubaneh Hemmati  <https://orcid.org/0000-0003-2226-5395>
 Justin Howell  <https://orcid.org/0000-0001-6028-8059>
 Rolf A. Jansen  <https://orcid.org/0000-0003-1268-5230>
 Zhiyuan Ji  <https://orcid.org/0000-0001-7673-2257>
 Sugata Kaviraj  <https://orcid.org/0000-0002-5601-575X>
 Keunho J. Kim  <https://orcid.org/0000-0001-6505-0293>
 Peter Kurczynski  <https://orcid.org/0000-0002-8816-5146>
 Ilin Lazar  <https://orcid.org/0009-0000-1797-0300>
 Ray A. Lucas  <https://orcid.org/0000-0003-1581-7825>

John MacKenty  <https://orcid.org/0000-0001-6529-8416>
 Kameswara Bharadwaj Mantha  <https://orcid.org/0000-0002-6016-300X>
 Alec Martin  <https://orcid.org/0000-0002-6632-4046>
 Garreth Martin  <https://orcid.org/0000-0003-2939-8668>
 Tyler McCabe  <https://orcid.org/0000-0002-5506-3880>
 Bahram Mobasher  <https://orcid.org/0000-0001-5846-4404>
 Alexa M. Morales  <https://orcid.org/0000-0003-4965-0402>
 Robert O'Connell  <https://orcid.org/0000-0002-8190-7573>
 Charlotte Olsen  <https://orcid.org/0000-0002-8085-7578>
 Lillian Ottosen  <https://orcid.org/0000-0001-9665-3003>
 Swara Ravindranath  <https://orcid.org/0000-0002-5269-6527>
 Caleb Redshaw  <https://orcid.org/0000-0002-9961-2984>
 Michael Rutkowski  <https://orcid.org/0000-0001-7016-5220>
 Brant Robertson  <https://orcid.org/0000-0002-4271-0364>
 Zahra Sattari  <https://orcid.org/0000-0002-0364-1159>
 Emmaris Soto  <https://orcid.org/0000-0002-2390-0584>
 Lei Sun  <https://orcid.org/0009-0004-6325-7839>
 Sina Taamoli  <https://orcid.org/0000-0003-0749-4667>
 Eros Vanzella  <https://orcid.org/0000-0002-5057-135X>
 L. Y. Aaron Yung  <https://orcid.org/0000-0003-3466-035X>
 Bonnabelle Zabelle  <https://orcid.org/0000-0002-7830-363X>

References

- Alavi, A., Siana, B., Richard, J., et al. 2014, *ApJ*, 780, 143
 Alavi, A., Siana, B., Richard, J., et al. 2016, *ApJ*, 832, 56
 Arnouts, S., Cristiani, S., Moscardini, L., et al. 1999, *MNRAS*, 310, 540
 Ashby, M. L. N., Willner, S. P., Fazio, G. G., et al. 2013, *ApJ*, 769, 80
 Ashby, M. L. N., Willner, S. P., Fazio, G. G., et al. 2015, *ApJS*, 218, 33
 Astropy Collaboration, Price-Whelan, A. M., Lim, P. L., et al. 2022, *ApJ*, 935, 167
 Astropy Collaboration, Price-Whelan, A. M., Sipőcz, B. M., et al. 2018, *AJ*, 156, 123
 Astropy Collaboration, Robitaille, T. P., Tollerud, E. J., et al. 2013, *A&A*, 558, A33
 Baldry, I. K., Driver, S. P., Loveday, J., et al. 2012, *MNRAS*, 421, 621
 Balestra, I., Mainieri, V., Popesso, P., et al. 2010, *A&A*, 512, A12
 Barger, A. J., Cowie, L. L., & Wang, W. H. 2008, *ApJ*, 689, 687
 Barmby, P., Huang, J. S., Ashby, M. L. N., et al. 2008, *ApJS*, 177, 431
 Barro, G., Pérez-González, P. G., Cava, A., et al. 2019, *ApJS*, 243, 22
 Benítez, N. 2000, *ApJ*, 536, 571
 Benítez, N., Ford, H., Bouwens, R., et al. 2004, *ApJS*, 150, 1
 Bezanson, R., Wake, D. A., Brammer, G. B., et al. 2016, *ApJ*, 822, 30
 Bielby, R., Hudelot, P., McCracken, H. J., et al. 2012, *A&A*, 545, A23
 Blanton, M. R., & Roweis, S. 2007, *AJ*, 133, 734
 Boogaard, L. A., Brinchmann, J., Bouché, N., et al. 2018, *A&A*, 619, A27
 Boquien, M., Burgarella, D., Roehly, Y., et al. 2019, *A&A*, 622, A103
 Bouwens, R. J., Illingworth, G. D., Oesch, P. A., et al. 2010, *ApJL*, 709, L133
 Brammer, G. B., van Dokkum, P. G., & Coppi, P. 2008, *ApJ*, 686, 1503
 Brammer, G. B., van Dokkum, P. G., Franx, M., et al. 2012, *ApJS*, 200, 13
 Bruzual, G., & Charlot, S. 2003, *MNRAS*, 344, 1000
 Burgarella, D., Buat, V., & Iglesias-Páramo, J. 2005, *MNRAS*, 360, 1413
 Byler, N., Dalcanton, J. J., Conroy, C., & Johnson, B. D. 2017, *ApJ*, 840, 44
 Calzetti, D., Armus, L., Bohlin, R. C., et al. 2000, *ApJ*, 533, 682
 Cardelli, J. A., Clayton, G. C., & Mathis, J. S. 1989, *ApJ*, 345, 245
 Chabrier, G. 2003, *PASP*, 115, 763
 Chabrier, G., Hennebelle, P., & Charlot, S. 2014, *ApJ*, 796, 75
 Coe, D., Benítez, N., Sánchez, S. F., et al. 2006, *AJ*, 132, 926
 Coil, A. L., Blanton, M. R., Burles, S. M., et al. 2011, *ApJ*, 741, 8
 Conroy, C., & Gunn, J. E. 2010a, *ApJ*, 712, 833
 Conroy, C., & Gunn, J. E. 2010b, FSPS: Flexible Stellar Population Synthesis, Astrophysics Source Code Library, ascl:1010.043
 Conroy, C., Gunn, J. E., & White, M. 2009, *ApJ*, 699, 486
 Cooper, M. C., Aird, J. A., Coil, A. L., et al. 2011, *ApJS*, 193, 14
 Cooper, M. C., Griffith, R. L., Newman, J. A., et al. 2012, *MNRAS*, 419, 3018
 Cristiani, S., Appenzeller, I., Arnouts, S., et al. 2000, *A&A*, 359, 489
 Croom, S. M., Smith, R. J., Boyle, B. J., et al. 2001, *MNRAS*, 322, L29
 Daddi, E., Cimatti, A., Renzini, A., et al. 2004, *ApJ*, 617, 746
 Dahlen, T., Mobasher, B., Faber, S. M., et al. 2013, *ApJ*, 775, 93

- Dale, D. A., Helou, G., Magdis, G. E., et al. 2014, *ApJ*, 784, 83
- Damjanov, I., Zahid, H. J., Geller, M. J., Fabricant, D. G., & Hwang, H. S. 2018, *ApJS*, 234, 21
- Davidzon, I., Ilbert, O., Laigle, C., et al. 2017, *A&A*, 605, A70
- Dickinson, M., Bergeron, J., Casertano, S., et al. 2003, Spitzer Proposal, 196
- Doherty, M., Bunker, A. J., Ellis, R. S., & McCarthy, P. J. 2005, *MNRAS*, 361, 525
- Domínguez, A., Siana, B., Brooks, A. M., et al. 2015, *MNRAS*, 451, 839
- Draine, B. T., & Li, A. 2007, *ApJ*, 657, 810
- Emami, N., Siana, B., Weisz, D. R., et al. 2019, *ApJ*, 881, 71
- Faber, S. 2011, The Cosmic Assembly Near-IR Deep Extragalactic Legacy Survey (“CANDELS”), MAST, doi:10.17909/T94S3X
- Fan, X., Strauss, M. A., Becker, R. H., et al. 2006, *AJ*, 132, 117
- Ferreras, I., Pasquali, A., Malhotra, S., et al. 2009, *ApJ*, 706, 158
- Fioc, M., & Rocca-Volmerange, B. 1997, *A&A*, 326, 950
- Fontana, A., D’Odorico, S., Poli, F., et al. 2000, *AJ*, 120, 2206
- Fontana, A., Dunlop, J. S., Paris, D., et al. 2014, *A&A*, 570, A11
- Giallongo, E., D’Odorico, S., Fontana, A., et al. 1998, *AJ*, 115, 2169
- Giavalisco, M., Ferguson, H. C., Koekemoer, A. M., et al. 2004, *ApJL*, 600, L93
- Grazian, A., Fontana, A., de Santis, C., et al. 2006, *A&A*, 449, 951
- Grazian, A., Giallongo, E., Paris, D., et al. 2017, *A&A*, 602, A18
- Grogin, N. A., Kocevski, D. D., Faber, S. M., et al. 2011, *ApJS*, 197, 35
- Guo, Y., Ferguson, H. C., Giavalisco, M., et al. 2013, *ApJS*, 207, 24
- Gwyn, S. D. J. 2012, *AJ*, 143, 38
- Harris, C. R., Millman, K. J., van der Walt, S. J., et al. 2020, *Natur*, 585, 357
- Hasinger, G., Capak, P., Salvato, M., et al. 2018, *ApJ*, 858, 77
- Hathi, N. P., Ferreras, I., Pasquali, A., et al. 2009, *ApJ*, 690, 1866
- Herenz, E. C., Urrutia, T., Wisotzki, L., et al. 2017, *A&A*, 606, A12
- Hildebrandt, H., Arnouts, S., Capak, P., et al. 2010, *A&A*, 523, A31
- Hopkins, A. M. 2018, *PASA*, 35, e039
- Hopkins, P. F., Kereš, D., Oñorbe, J., et al. 2014, *MNRAS*, 445, 581
- Hsu, L.-T., Lin, L., Dickinson, M., et al. 2019, *ApJ*, 871, 233
- Huang, J. S., Faber, S. M., Daddi, E., et al. 2009, *ApJ*, 700, 183
- Hunter, J. D. 2007, *CSE*, 9, 90
- Ilbert, O., Arnouts, S., McCracken, H. J., et al. 2006, *A&A*, 457, 841
- Ilbert, O., Capak, P., Salvato, M., et al. 2009, *ApJ*, 690, 1236
- Inami, H., Bacon, R., Brinchmann, J., et al. 2017, *A&A*, 608, A2
- Inoue, A. K. 2011, *MNRAS*, 415, 2920
- Iyer, K., & Gawiser, E. 2017, *ApJ*, 838, 127
- Iyer, K. G., Gawiser, E., Faber, S. M., et al. 2019, *ApJ*, 879, 116
- Jain, S., Tacchella, S., & Mosleh, M. 2024, *MNRAS*, 527, 3291
- Kajisawa, M., Ichikawa, T., Tanaka, I., et al. 2011, *PASJ*, 63, 379
- Kaushal, Y., Nersesian, A., Bezanson, R., et al. 2024, *ApJ*, 961, 118
- Kodra, D., Andrews, B. H., Newman, J. A., et al. 2023, *ApJ*, 942, 36
- Koekemoer, A. M., Faber, S. M., Ferguson, H. C., et al. 2011, *ApJS*, 197, 36
- Kriek, M., Shapley, A. E., Reddy, N. A., et al. 2015, *ApJS*, 218, 15
- Kroger, J. K., Zirm, A. W., Toft, S., Man, A., & Brammer, G. 2014, *ApJ*, 797, 17
- Kurczynski, P., Gawiser, E., Acquaviva, V., et al. 2016, *ApJL*, 820, L1
- Kurk, J., Cimatti, A., Daddi, E., et al. 2013, *A&A*, 549, A63
- Laidler, V. G., Papovich, C., Grogin, N. A., et al. 2007, *PASP*, 119, 1325
- Le Fèvre, O., Cassata, P., Cucciati, O., et al. 2013, *A&A*, 559, A14
- Le Fèvre, O., Tasca, L. A. M., Cassata, P., et al. 2015, *A&A*, 576, A79
- Leja, J., Camall, A. C., Johnson, B. D., Conroy, C., & Speagle, J. S. 2019, *ApJ*, 876, 3
- Lilly, S. J., Le Brun, V., Maier, C., et al. 2009, *ApJS*, 184, 218
- Lilly, S. J., Le Fèvre, O., Renzini, A., et al. 2007, *ApJS*, 172, 70
- Lower, S., Narayanan, D., Leja, J., et al. 2020, *ApJ*, 904, 33
- Madau, P. 1995, *ApJ*, 441, 18
- Madau, P., & Dickinson, M. 2014, *ARA&A*, 52, 415
- Maraston, C. 2005, *MNRAS*, 362, 799
- Marchesini, D., van Dokkum, P. G., Förster Schreiber, N. M., et al. 2009, *ApJ*, 701, 1765
- Masters, D. C., Stern, D. K., Cohen, J. G., et al. 2019, *ApJ*, 877, 81
- McCracken, H. J., Milvang-Jensen, B., Dunlop, J., et al. 2012, *A&A*, 544, A156
- McLure, R. J., Pentericci, L., Cimatti, A., et al. 2018, *MNRAS*, 479, 25
- Mehta, V., Scarlata, C., Capak, P., et al. 2018, *ApJS*, 235, 36
- Mehta, V., Scarlata, C., Rafelski, M., et al. 2017, *ApJ*, 838, 29
- Mehta, V., Teplitz, H. I., Scarlata, C., et al. 2023, *ApJ*, 952, 133
- Meiksin, A. 2006, *MNRAS*, 365, 807
- Mérida, R. M., Pérez-González, P. G., Sánchez-Blázquez, P., et al. 2023, *ApJ*, 950, 125
- Mignoli, M., Cimatti, A., Zamorani, G., et al. 2005, *A&A*, 437, 883
- Momcheva, I. G., Brammer, G. B., van Dokkum, P. G., et al. 2016, *ApJS*, 225, 27
- Morishita, T., Abramson, L. E., Treu, T., et al. 2017, *ApJ*, 835, 254
- Moutard, T., Sawicki, M., Arnouts, S., et al. 2020, *MNRAS*, 494, 1894
- Muzzin, A., Marchesini, D., Stefanon, M., et al. 2013, *ApJ*, 777, 18
- Nayyeri, H., Hemmati, S., Mobasher, B., et al. 2017, *ApJS*, 228, 7
- Nedkova, K. V., Häußler, B., Marchesini, D., et al. 2021, *MNRAS*, 506, 928
- Nedkova, K. V., Rafelski, M., Teplitz, H. I., et al. 2024, *ApJ*, 970, 188
- Newman, J. A., Cooper, M. C., Davis, M., et al. 2013, *ApJS*, 208, 5
- Noll, S., Burgarella, D., Giovannoli, E., et al. 2009, *A&A*, 507, 1793
- Nonino, M., Dickinson, M., Rosati, P., et al. 2009, *ApJS*, 183, 244
- Oke, J. B., & Gunn, J. E. 1983, *ApJ*, 266, 713
- Pacifici, C., Iyer, K. G., Mobasher, B., et al. 2023, *ApJ*, 944, 141
- Pasquali, A., Ferreras, I., Panagia, N., et al. 2006, *ApJ*, 636, 115
- Pentericci, L., McLure, R. J., Garilli, B., et al. 2018, *A&A*, 616, A174
- Picouet, V., Arnouts, S., Le Floc’h, E., et al. 2023, *A&A*, 675, A164
- Planck Collaboration, Ade, P. A. R., Aghanim, N., et al. 2016, *A&A*, 594, A13
- Prevot, M. L., Lequeux, J., Maurice, E., Prevot, L., & Rocca-Volmerange, B. 1984, *A&A*, 132, 389
- Rafelski, M., Teplitz, H. I., Gardner, J. P., et al. 2015, *AJ*, 150, 31
- Rafelski, M., Wolfe, A. M., Cooke, J., et al. 2009, *ApJ*, 703, 2033
- Ravikumar, C. D., Puech, M., Flores, H., et al. 2007, *A&A*, 465, 1099
- Retzlaff, J., Rosati, P., Dickinson, M., et al. 2010, *A&A*, 511, A50
- Riess, A. G., Strolger, L.-G., Casertano, S., et al. 2007, *ApJ*, 659, 98
- Roche, N. D., Dunlop, J., Caputi, K. I., et al. 2006, *MNRAS*, 370, 74
- Sanders, D. B., Salvato, M., Aussel, H., et al. 2007, *ApJS*, 172, 86
- Santini, P., Fontana, A., Grazian, A., et al. 2009, *A&A*, 504, 751
- Schlegel, D. J., Finkbeiner, D. P., & Davis, M. 1998, *ApJ*, 500, 525
- Scoville, N., Aussel, H., Brusa, M., et al. 2007, *ApJS*, 172, 1
- Shen, S., Mo, H. J., White, S. D. M., et al. 2003, *MNRAS*, 343, 978
- Silverman, J. D., Kashino, D., Sanders, D., et al. 2015, *ApJS*, 220, 12
- Skelton, R. E., Whitaker, K. E., Momcheva, I. G., et al. 2014, *ApJS*, 214, 24
- Speagle, J. S., Steinhardt, C. L., Capak, P. L., & Silverman, J. D. 2014, *ApJS*, 214, 15
- Stanford, S. A., Masters, D., Darvish, B., et al. 2021, *ApJS*, 256, 9
- Stefanon, M., Yan, H., Mobasher, B., et al. 2017, *ApJS*, 229, 32
- Straughn, A. N., Pirzkal, N., Meurer, G. R., et al. 2009, *AJ*, 138, 1022
- Strolger, L.-G., Riess, A. G., Dahlen, T., et al. 2004, *ApJ*, 613, 200
- Sun, G., Faucher-Giguère, C.-A., Hayward, C. C., et al. 2023, *ApJL*, 955, L35
- Sun, L., Wang, X., Teplitz, H. I., et al. 2024, *ApJ*, 972, 8
- Taniguchi, Y., Kajisawa, M., Kobayashi, M. A. R., et al. 2015, *PASJ*, 67, 104
- Taniguchi, Y., Scoville, N., Murayama, T., et al. 2007, *ApJS*, 172, 9
- Teplitz, H. I., Rafelski, M., Kurczynski, P., et al. 2013, *AJ*, 146, 159
- Treister, E., Virani, S., Gawiser, E., et al. 2009, *ApJ*, 693, 1713
- Trump, J. R., Impey, C. D., Elvis, M., et al. 2009, *ApJ*, 696, 1195
- Trump, J. R., Konidaris, N. P., Barro, G., et al. 2013, *ApJL*, 763, L6
- Trump, J. R., Sun, M., Zeimann, G. R., et al. 2015, *ApJ*, 811, 26
- Trump, J. R., Weiner, B. J., Scarlata, C., et al. 2011, *ApJ*, 743, 144
- van der Wel, A., Franx, M., van Dokkum, P. G., et al. 2005, *ApJ*, 631, 145
- van der Wel, A., Noeske, K., Bezanson, R., et al. 2016, *ApJS*, 223, 29
- Vanzella, E., Cristiani, S., Dickinson, M., et al. 2008, *A&A*, 478, 83
- Vanzella, E., Giavalisco, M., Dickinson, M., et al. 2009, *ApJ*, 695, 1163
- Virtanen, P., Gommers, R., Oliphant, T. E., et al. 2020, *NatMe*, 17, 261
- Wang, X., Teplitz, H. I., Sun, L., et al. 2024, *RNAAS*, 8, 26
- Weaver, J. R., Davidzon, I., Toft, S., et al. 2023, *A&A*, 677, A184
- Weibel, A., Oesch, P. A., Baruffet, L., et al. 2024, *MNRAS*, 533, 1808
- Weiner, B. 2009, HST Proposal, 11600
- Weisz, D. R., Johnson, B. D., Johnson, L. C., et al. 2012, *ApJ*, 744, 44
- Whitaker, K. E., Franx, M., Leja, J., et al. 2014, *ApJ*, 795, 104
- Whitaker, K. E., Labbé, I., van Dokkum, P. G., et al. 2011, *ApJ*, 735, 86
- Windhorst, R. A., Cohen, S. H., Hathi, N. P., et al. 2011, *ApJS*, 193, 27
- Wirth, G. D., Trump, J. R., Barro, G., et al. 2015, *AJ*, 150, 153
- Wolf, C., Meisenheimer, K., Kleinheinrich, M., et al. 2004, *A&A*, 421, 913
- Wuyts, S., Labbé, I., Förster Schreiber, N. M., et al. 2008, *ApJ*, 682, 985
- Wuyts, S., van Dokkum, P. G., Franx, M., et al. 2009, *ApJ*, 706, 885
- Xue, Y. Q., Luo, B., Brandt, W. N., et al. 2016, *ApJS*, 224, 15
- Yoshikawa, T., Akiyama, M., Kajisawa, M., et al. 2010, *ApJ*, 718, 112